In: Monomers, Oligomers, Polymers, Composites… ISBN: 978-1-60456-877-6
Editors: R. A. Pethrick, G.E. Zaikov et al.

Chapter 10

ADVANCES IN HEAT AND FLUID FLOW COMPUTATIONAL TECHNIQUES WITH PARTICULAR REFERENCE TO MICROCHANNELS AS POROUS MEDIA

N. Amanifard and A. K. Haghi*
University of Guilan, P. O. Box 3756, Rasht, Iran

ABSTRACT

In this chapter advances in heat and fluid flow computational techniques with particular application in microchannels is introduced. Throughout the chapter, the flow and heat transfer development regions inside the channels are considered. The numerical results are then compared with the available experimental data. The effects of liquid velocity through channels and their effects on heat transfer and pressure drop along microchannels are investigated. Finally, the effects of aspect ratio on heat dissipation and pressure drop in microchannels are discussed and predicted.

NOMECLATURE

C_{pf} Specified heat capacity of the cooling liquid [j kg^{-1} k^{-1}]
D_h Hydraulic diameter [m]
e Elementary charge [C]
E_x Streaming potential [v/m]
$\overline{E}_x$ Non-dimensional Streaming potential
$\overline{G}$ Non-dimensional parameter
H_t Height of microchannel [m]
H_c Depth of microchannel [m]

* Corresponding author e-mail: Haghi@Guila.ac.ir

k Non-dimensional electrokinetic diameter
k_b Boltzman constant [j mol^{-1} k^{-1}]
k_f Thermal conductivity of cooling liquid [w m^{-1} k^{-1}]
k Thermal conductivity of silicon[w m^{-1} k^{-1}]
k_f Thermal conductivity of fluid phase [w m^{-1} k^{-1}]
k_s Thermal conductivity of solid phase [w m^{-1} k^{-1}]
L Total length of microchannel [m]
n_{io} Bulk concentration of type-I ion [m^{-3}]
$\overline{P}$ Non-dimensional pressure
q Heat flux [w m^{-2}]
R Thermal resistance [m^2 k w^{-1}]
Re Reynolds number
T Absolute temperature [k]
T_{out} Measured outlet temperature [k]
T_{in} Measured inlet temperature [k]
T_f Fluid temperature [k]
$\tilde{T}_f$ Volume –averaged fluid temperature [k]
$\overline{T}_f$ Mean fluid temperature [k]
T_s Solid phase temperature
u Velocity in X-direction [ms^{-1}]
u Velocity vector [ms^{-1}]
$\tilde{u}$ Volume-averaged velocity in x-direction[ms^{-1}]
v Velocity in Y-direction [ms^{-1}]
w Velocity in Z-direction [ms^{-1}]
$\overline{u}$ Non-dimensional Velocity in X-direction
W_c Width of microchannel [m]
W_s Wall thickness of microchannel [m]
W_t Total width of microchannel [m]
x_i General coordinate
x x- coordinate
y y- coordinate
z z- coordinate
Y Non-dimensional coordinate
Z Non-dimensional coordinate
Z_i Valence of type-i ion

Greek Symbols

α The aspect ratio of the channels
α_f Thermal diffusivity of the cooling liquid [wkm^2]

ε Porosity

ε_r Dielectric constant of the liquid

ε_0 Permittivity of vacuum [$CV^{-1}m^{-1}$]

θ Dimensionless temperature of cooling liquid [k]

$\aleph$ Debye-Huckel parameter [m^{-1}]

ζ Zeta potential [V]

$\overline{\zeta}$ Non-Dimensional zeta potential

ρ_f Density of cooling liquid [kg m^{-3}]

ρ_e Net volume charge density [C m^{-3}]

ψ Electric potential [V]

Ψ Non-Dimensional Electric potential

1. INTRODUCTION

With the advances in computing technology over the past few decades, electronics have become faster, smaller and more powerful. This results in an ever-increasing heat generation rate from electronic devices. In most cases, the chips are cooled using forced air flow. However, when dealing with a component that contains billions of transistors working at high frequency, the temperature can reach a critical level where standard cooling methods are not sufficient. In addition to high-performance electronic chips, high heat flux removal is also required in devices such as laser diode arrays and high-energy mirrors. In the last two decades, many cooling technologies have been pursued to meet the high heat dissipation rate requirements and maintain a low junction temperature. Among these efforts, the microchannel heat sink (MCHS) has received much attention because of its ability to produce high heat transfer coefficient, small size and volume per heat load, and small coolant requirements (Tsai and Chein (2007)). (See figure 1)

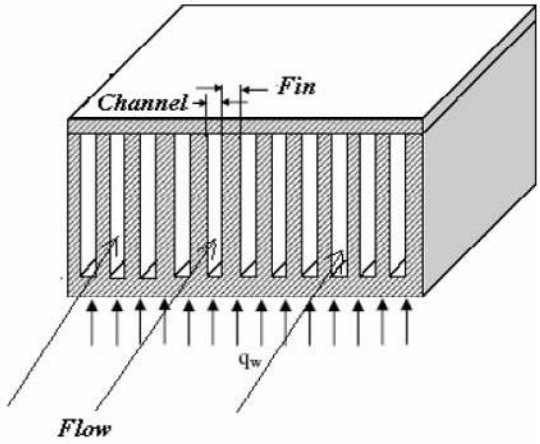

Figure 1. An schematic shape of a Microchannel.

The MCHS cooling concept was proposed by Tuckerman and Pease (1981). Since then, MCHS performances with different substrate materials and channel dimensions have been studied extensively in the past two decades. These studies can be categorized into theoretical (Knight et al., 1992; Ambatipudi and Rahman, 2000), numerical (Fedorov and Viskanta, 2000; Lee et al., 2005; Li et al., 2004; Li and Peterson, 2006; Amanifard and Haghi., 2006; Amanifard et al., 2007; Amanifard and Haghi, 2007), and experimental approaches (Qu and Mudawar, 2002; Tiselj et al., 2004).

In the theoretical approach, most studies employed the classical fin theory which models the solid walls separating microchannels as thin fins. The heat transfer process is simplified as one-dimensional, constant convection heat transfer coefficient and uniform fluid temperature, and these assumptions make validity of this approach in a limited range. The fin approach is effective for the analysis of micro-scale heat transfer in many practical applications, and has been used recently to investigate the efficiency of micro-cell honeycombs in compact heat exchangers (Lu, 1999), and the design of cellar metal system (Gu et al., 2001).However, the nature of the heat transfer process in MCHS is conjugated heat conduction in the solid wall and convection to the cooling fluid. The simplifications used in the theoretical approach usually under- or over predict MCHS performance. To overcome the shortcomings associated with MCHS thermal performance analysis using fin theory, several investigators proposed modeling the MCHS as a porous medium. Kohen and colony (1986) modeled the microchannels as a porous medium by using Darcy's law to describe the flow. Later, Tien and Kuo (1987) analyzed the convection heat transfer in microstructures by using the Brinkman-extended Darcy model for fluid flow to impose the boundary layer effects, and the Forchheimer-Brinkman-extended Darcy equation proposed by Vafai and Tien (1981) for porous mediums. More recently, Kim and Kim (1999) analyzed the laminar heat transfer in MCHS using a modified Darcy model for fluid flow and two-equation model for heat transfer. They found that their results agreed well with those predicted using fin theory models (Knight et al., 1992) and experimental measurements by Tuckerman and Pease (1981). Zhao and Lu (2002) further extended the model developed by Kim and Kim (1999) to study the channel geometries, effective thermal conductivities and porosities on MCHS thermal performance (figure 2 Shows the equivalent porous media).

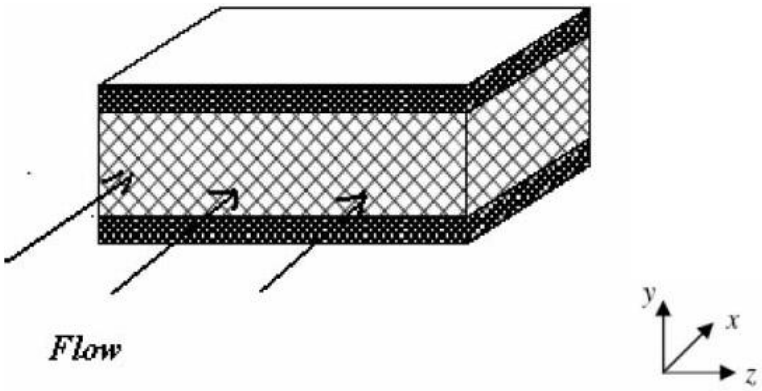

Figure 2. The equivalent Microchannel as a porous media.

Because conjugated heat transfer is involved in MCHS, it is believed that the porous medium model is better than the classical fin theory in describing MCHS thermal performance, and upon this basic idea, the microchannel studies become as a branch of porous media heat transfer problems.

2. THE CONTINUITY APPROACH OF MICROCHANNELS

2.1. Flow without Electric Field

The fin physical approach relies on continuity concepts and the Navier-Stokes equations with the energy equation are solved with no-slip boundary condition and the viscous dissipation effects without any electric field on walls. Wu and Little (1983) measured the heat transfer characteristics for gas flows in miniature channels with inner diameter ranging from 134 to 164 μm. The tests involved both laminar and turbulent flow regimes. Their results showed that the turbulent convection occurs at Reynold's number of approximately 1000. They also found that the convective heat transfer characteristics depart from the predictions of the established empirical correlations for the macroscale tubes. They attributed these deviations to the large asymmetric relative roughness of the microchannel walls.

Harms et al. (1997) tested a 2.5 cm long, 2.5 cm wide silicon heat sink having 251μm wide and 1030 μm deep microchannels. A relatively low Reynolds number of 1500 marked transition from laminar to turbulent flow which was attributed to a sharp inlet, relatively long entrance region, and channel surface roughness. They concluded the classical relation for Nusselt number was fairly accurate for modeling microchannel flows.

Fedrov and Viskanta (2000) reported that the thermal resistance decreases when Reynolds number increases and approaches an asymptote at high Reynolds numbers.

Choi et al. (1991) measured the convective heat transfer coefficients for flow of nitrogen gas in microtubes for both laminar and turbulent regimes. They found that the measured Nusselt number in laminar flow exhibits a Reynolds number dependence in contrast with the conventional prediction for the fully developed laminar flow, in which Nusselt number is constant.

Adam et al. (1998)conducted single-phase flow studies in microchannel using water as the working fluid. Two diameters of the circular microchannels, namely 0.76 mm and 1.09 mm, were used in the investigation. It was found that the Nusselt numbers are larger than those encountered in macrochannels.

Peng and Peterson (1996) investigated water flows in rectangular microchannels with hydraulic diameters ranging from 0.133 to 0.336 mm. In laminar flows, it was found that the heat transfer depends on the aspect ratio and the ratio of the hydraulic diameter to the center-to-center distance of the microchannel.

Computational Model

The physical characteristics of a computational model for the fin approach are illustrated in figure 3.

The width and the height of the microchannels are W_s, and H_c respectively. The thickness of the substructure is $H_t - H_c$; and the total length of the microchannels is *L*.

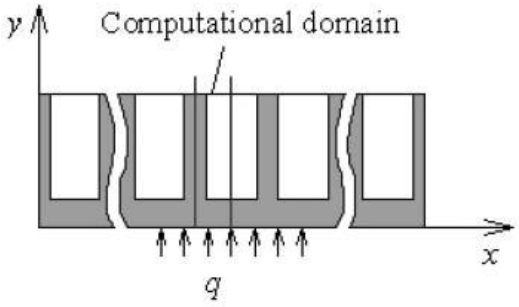

a

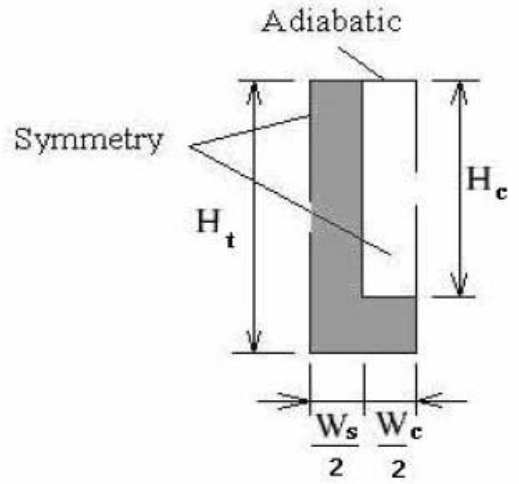

b

Figure 3. Dimensions of the computational model.

Governing Equations

Several simplifying assumptions are incorporated before establishing the governing equations for the fluid flow and heat transfer in the unit cell:

1. Steady fluid flow and heat transfer;
2. Incompressible fluid;
3. Laminar flow;
4. Negligible radiative heat transfer;
5. Constant solid and fluid properties except water viscosity.

However, the variation of water viscosity is significant. Therefore, a polynomial function in a limited temperature range is usually considered for the viscosity variations.

$$\mu(T) = a + bT + cT^2 + dT^3 + eT^4 + fT^5 \quad (1)$$

The coefficients of the above equation are given in table 1.

Table 1. Coefficients of the polynomial function

a	b	c	d	e	f
0.5779	-0.0078	4.E-05	-1E-07	2.E-10	-9.E-14

Based on the above assumptions, the governing differential equations used to describe the fluid flow and heat transfer in the unit cell of a microchannel can be proposed on the continuity basis.

Continuity

$$\frac{\partial u_i}{\partial x_i} = 0 \tag{2}$$

Momentum

$$\rho \frac{\partial (u_i u_j)}{\partial x_j} = -\frac{\partial P}{\partial x_i} + \mu \frac{\partial}{\partial x_j}\left(\frac{\partial u_i}{\partial x_j} + \frac{\partial u_j}{\partial x_i}\right) - \frac{2}{3}\mu \frac{\partial}{\partial x_i}\left(\frac{\partial u_k}{\partial x_k}\right) \tag{3}$$

Energy

$$\rho C_p \frac{\partial u_i T}{\partial x_i} = k \frac{\partial^2 T}{\partial x_i^{\,2}} + \mu \Phi \tag{4}$$

where

$$\Phi = 2\left[\left(\frac{\partial u}{\partial x}\right)^2 + \left(\frac{\partial v}{\partial y}\right)^2 + \left(\frac{\partial w}{\partial z}\right)^2\right] + \left(\frac{\partial u}{\partial y} + \frac{\partial v}{\partial x}\right)^2 + \left(\frac{\partial u}{\partial z} + \frac{\partial w}{\partial x}\right)^2 + \left(\frac{\partial v}{\partial z} + \frac{\partial w}{\partial y}\right)^2 \tag{5}$$

Flow Characteristics through a Specified Microchannel

The general solution of the fin theory can not be achieved by analytical methods, and the only way is the numerical analysis. Amanifard and Haghi (2006) performed a numerical solution for a specified microchannel which is used for cooling of a supercomputer chip.

The heat supplies by a 1cm × 1cm heat source located at the entrance of the microchannels and is centered across the whole channel heat sink. A uniform heat flux of q is provided to heat the microchannels. The heat is removed by flowing water through channels. The inlet temperature of the cooling water is $20°C$. The analysis is performed for four different cases. The dimensions related to each case are given in table 1.By these dimensions, there will be 150 microchannels for cases 0 and 1 and 200 microchannels for cases 2, 3, and 4.

Table 2. Four different cases for the microchannels

	Case				
	0	1	2	3	4
L(cm)	2	2	1.4	1.4	1.4
W_s (μm)	64	64	56	55	50
W_c(μm)	36	36	44	45	50
H_c(μm)	280	280	320	287	302
H_t(μm)	489	489	533	430	458
$\dot{Q}(cm^3/s)$	1.277	1.86	4.7	6.5	8.6
q(W/cm^2)	34.6	34.6	181	277	790
Number of channels	150	150	200	200	200

Boundary Conditions

The whole substructure is made of silicon with thermal conductivity (k) of $148W/m.K$. At the top of the channel $y = H_t$ is a pyrex plate to make an adiabatic condition (its thermal conductivity is two orders lower than silicon). There are two different boundary conditions at the bottom. For $z < L_h$ a uniform heat flux of q is imposed over the heat sink and the rest is assumed to be adiabatic. Water flows through the channel from the entrance in z direction. The transverse velocities of the inlet are assumed to be zero. The axial velocity is considered to be evenly distributed through the whole microchannel. The velocities at the top and the bottom of channels are zero.

Numerical Method

The Finite Volume Method (FVM) is used to solve the continuity, momentum, and energy equations. A brief description of the method is explained here.

In this method the domain is divided into a number of control volumes such that there is one control volume surrounding each grid point. The grid point is located in the center of a control volume. The governing equations are integrated over the individual control volumes to construct algebraic equations for the discrete dependent variables such as velocities, pressure, and temperature. Then the discretized equations express the conservation principle for a finite control volume just as the partial differential equations express for an infinitesimal control volume. Amanifar and Haghi (2006) Performed the solution be converged when the mass imbalance in the continuity equation is less than 10^{-6}.

Temperature and Velocity Profiles

Thermal specifications and the flow characteristics are the main parameters in microchannel design. The results of the mentioned problem are focused on these fields.

For solving the equations several grid structures were used. The grid density of 120×40×20 in z, y, and x directions is considered to be appropriate.

The thermal resistance is introduced as:

$$R(z) = \frac{T_{out} - T_{\text{in}}}{q} \tag{5}$$

Moreover, the Reynolds number is calculated as:

$$\text{Re} \equiv \frac{\rho w_{ave} D_h}{\mu} \tag{6}$$

Where the hydraulic diameter is defined as:

$$D_h \equiv \frac{4A}{P} = \frac{2H_1 W_1}{H_1 + W_1} \tag{7}$$

Temperature Distribution and Thermal Resistance

The temperature distributions at four *x-y* cross sections along the channel are shown in figure 4 for the Case 0. The four sections ($z_=$ 1, 3, 6, 9mm) are all in the heated area. The temperature contours are clustered at the entrance of the channels. This means that the heat removing (cooling) rate is higher at the entrance than the other parts of the channel.

The thermal resistance along the channel is shown in figure 5 for Cases 0 and 1. It can be seen that the thermal resistance has increased by increasing the *z* value and approaches to a maximum value at *z* = 9mm. The adequate consistency with respect to Tuckerman's experimental results (1984) is achieved. The maximum thermal resistance occurred in *z* = 9mm which is consistent with Tuckerman's results (1984). For the other Cases, The results are given in table 3. The computed resistances have acceptable values, except in Case 4, in which the error is noticeable. This may be due to the very large heat flux exposed to the heat sink, the prediction of large heat fluxes in micro-scales needs some modifications in fundamental approaches.

Table 6. Thermal resistance comparison

Case	$q(\frac{W}{cm^2})$	$R(cm^2K/W)$		Error (%)
		Experimental	Numerical	
0	34.6	0.277	0.253	8.5
1	34.6	0.28	0.246	12.1
2	181	0.110	0.116	5
3	277	0.113	0.101	8.1
4	790	0.090	0.086	3.94

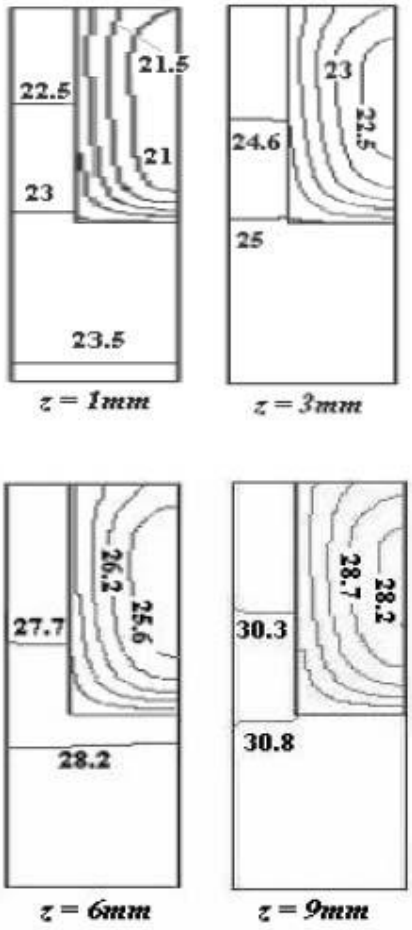

Figure 4. Temperature distribution along the channel for Case 0.

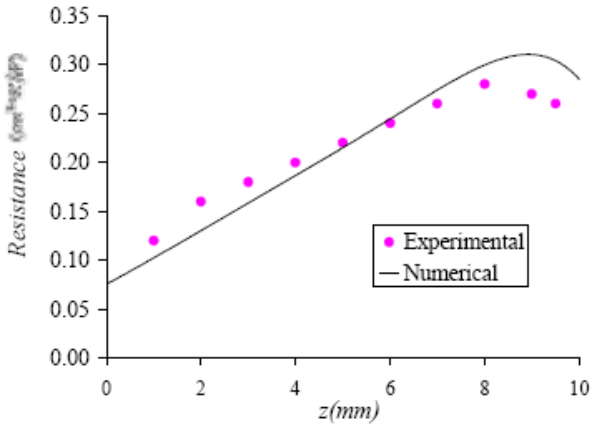

a

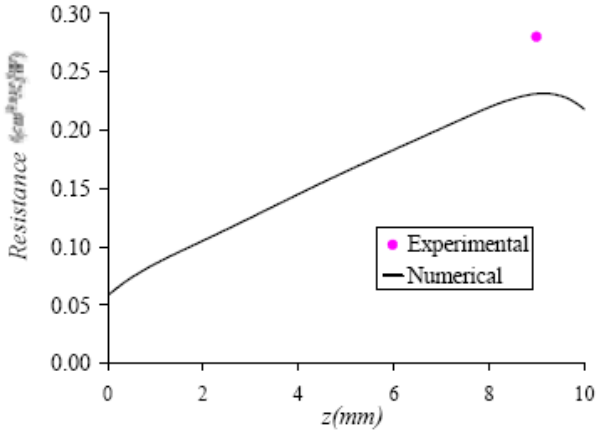

b

Figure 5. Numerical and experimental Thermal resistances for: (a) Case 0, and (b) Case 1.

Velocity Distribution

Figure 6 illustrates the velocity profiles in various *y-z* sections in Cases 0 and 1. It is obvious that, the velocity gradients near the channel walls are very large. This means that the wall shear stress is considerably large and consequently, the pressure drop along the channel becomes significant. Although the thermal boundary layer through the channel is fully developed, but the fully developed velocity is not valid and the velocity profile through whole channel does not reaches the developed form.

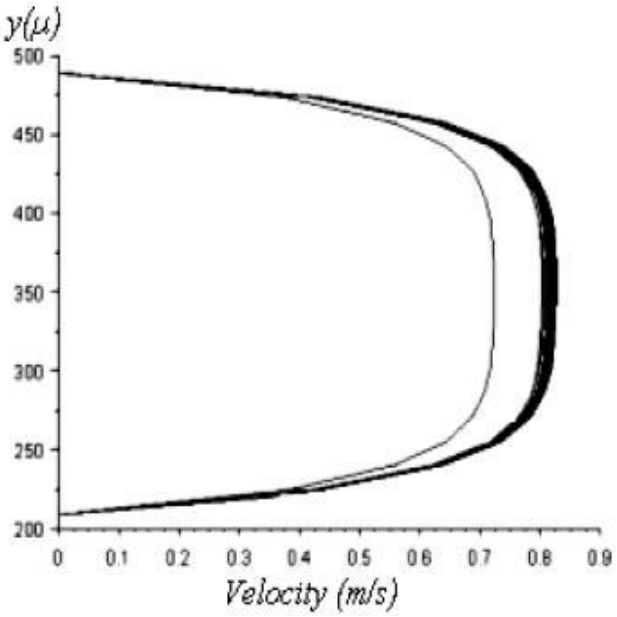

a

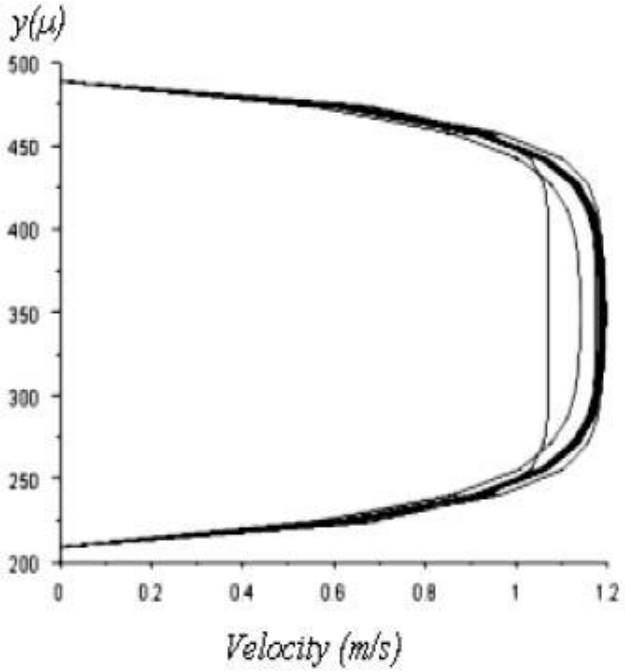

b

Figure 6. Velocity profiles in *y-z* sections, (a) Case 0, (b)Case 1.

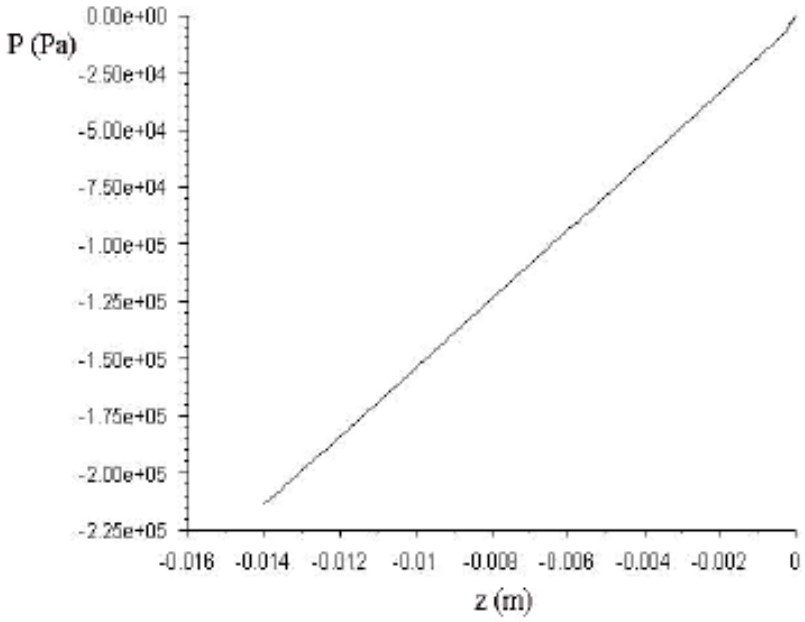

a

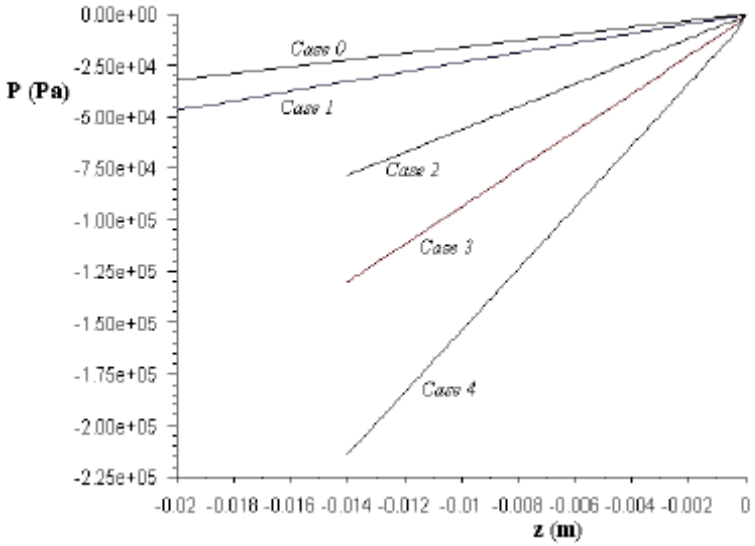

b

Figure 7. Pressure drop curves, (a) case 4, (b) all cases.

Pressure Drop

Figure 7(a) shows the pressure drop for the case 4 and figure 7(b) gives a comparison of the pressure drops for all study cases. As mentioned, the high level of the pressure drop relates to the high levels of the wall shear stresses.

These amounts are tabulated in table 4.

Table 4. Pressure drop in 5 Cases

Case	Pressure Drop (bar)
0	0.322
1	0.469
2	0.784
3	1.302
4	2.137

The Effect of Velocity on Temperature Distribution and Pressure Drop

The effects of velocity on the temperature rise and pressure drop in microchannels are illustrated in figures 8 and 9. The amount of heat dissipation increases by increasing the entrance velocity values. It also can be seen that the reduction in temperature values goes down drastically by augment in velocity levels.

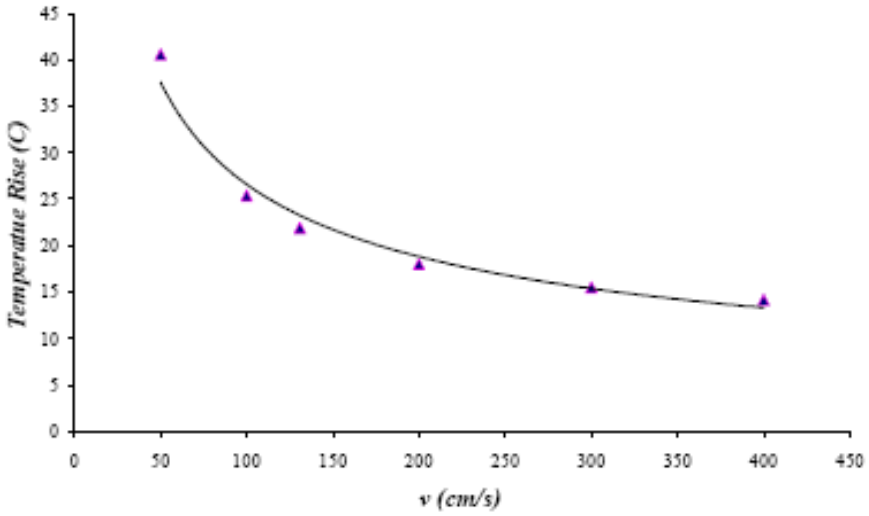

Figure 8. Temperature rise for different velocities.

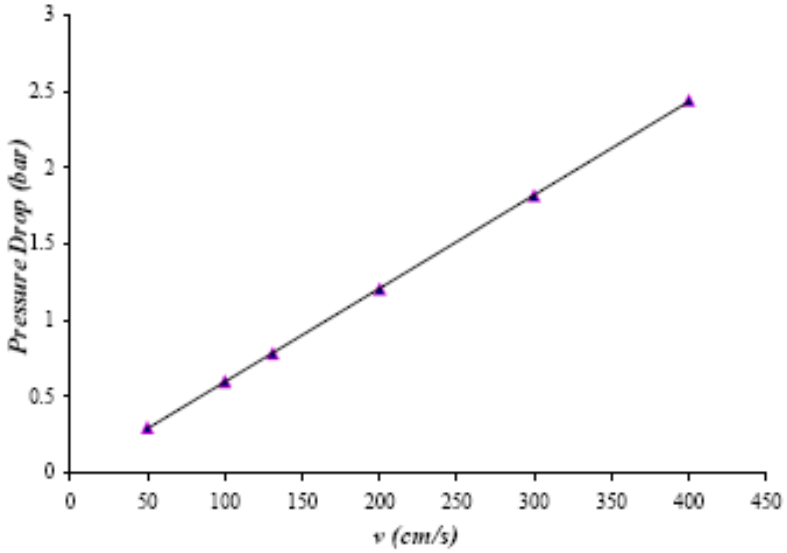

Figure 9. Pressure drop for different velocities.

A prediction empirical formula between the temperature and the velocity values was performed by Amanifard and Haghi (2006).

$$(T_{\max} - T_{in}) = 265.67u^{-0.4997} \tag{7}$$

The amounts of temperature rise and pressure drop are given in table 5.

Table 5. Temperature rise and pressure drop

Velocity (cm/s)	Re	Temp. Rise (°C)	Pressure Drop (bar)
50	47	40.6	0.298
100	95	25.4	0.598
131	124	21.9	0.784
200	190	18.0	1.206
300	285	15.5	1.817
400	380	14.2	2.439

The Effect of Aspect Ratio on Temperature Distribution and Pressure Drop

Aspect ratio is an important factor in microchannel design. In the current case the inlet heat flux of *181 W/cm*^{2} imposed over the heat sinks and the hydraulic diameter changes between 85.8 and 104.2. Figure 10 shows the maximum temperature of each case. It may be seen that with an identical heat flux the heat dissipation of the largest aspect ratio is the lowest. But this case has the minimum pressure drop too (figure 11). When the aspect ratio grows the heat dissipation increases. The third geometry has the minimum temperature rise. The temperature rise of the second and the forth geometries are approximately similar. On the other hand, the pressure drop of these two cases has a noticeable difference. The pressure drop increases with growth of the aspect ratio. The temperature levels of all geometries are given in table 6.

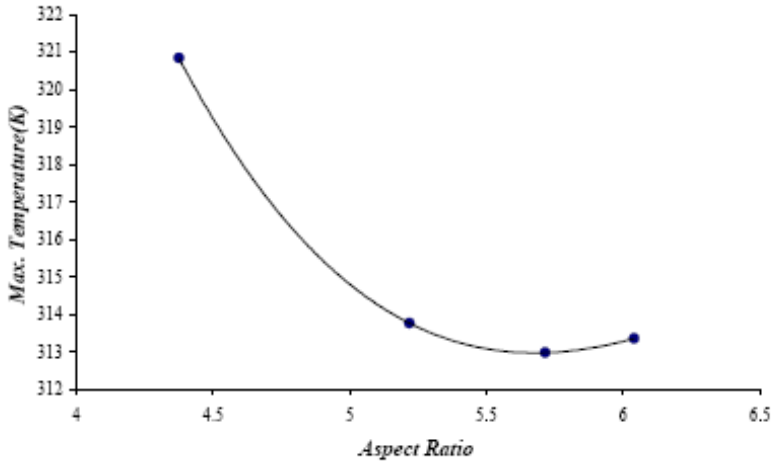

Figure 10. Max. temperature with respect to aspect ratio.

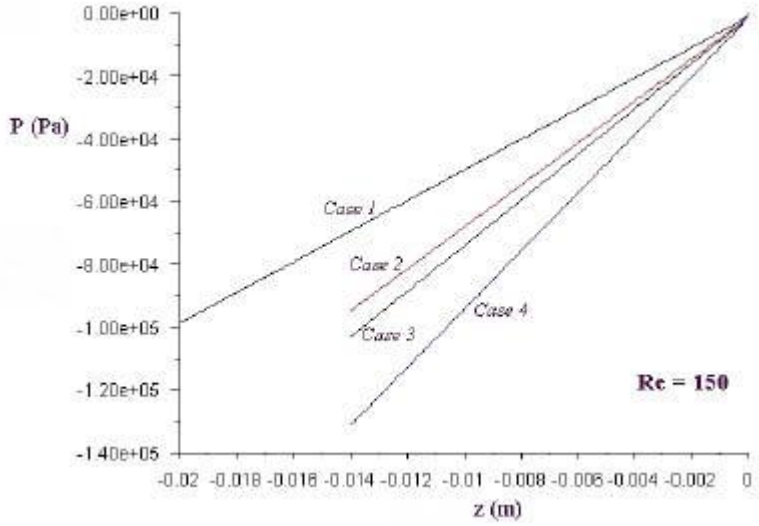

Figure 11. Pressure drop relating to each geometry in constant Reynolds of 150.

Table 6. Temperature rise and pressure drop for section 3

Case	Aspect Ratio	Hydraulic Diameter (μm)	Velocity (m/s)	Temp. Rise (°C)	Pressure Drop (bar)
1	4.375	104.19	1.447	27.84	0.98
2	5.714	95.32	1.58	19.97	0.95
3	5.218	92.31	1.633	20.76	1.03
4	6.040	85.80	1.76	20.35	1.31

The results gave the required assurance of using the full Navier-Stokes approach for the microchannels with aspect ratios about 0.1. However, for lower aspect ratios in the range of molecular mean free paths length scales, some modifications must be prepared for the boundary conditions and physical approaches (Mentioned in previous chapters on convection aspects).

2.2. The Continuity Approach with Electric Double Layer (EDL)

One possible explanation for these observed effects is the presence of the interfacial effects such as electric double layer, EDL. These effects are ignored in macro-scale fluid studies. Mala et al. (1996) considered the electrical body force resulting from the double layer field in the equations of motion. These equations were solved for the steady state flow. It was found that without the double layer a higher heat transfer rate is obtained. They proposed to consider the effects of the EDL on liquid flows and heat transfer in microchannels to prevent the overestimation of the heat transfer capacity of the system. Amanifard et al. (2007) completed their study (Amanifard and Haghi (2006)) by applying the EDL source terms in

governing equations (2)-(5) and gave a complete illustration of EDL effects on microchannel cases.

EDL Equations

Most of solid surfaces convey a static electric charge. In other words they will have superficial electric potential. If the liquid contains a very small number of ions (for instance, due to impurity), the electrostatic charges on the non-conducting solid surface will captivate the counter ions, and repel similar ions in cooling fluid. Consequently, as we can see in figure 12, the ions near the solid surface will found a new arrangement. The rearrangement of the charges on the solid surface and the balancing charges in the fluid is called the electric double layer. On the basis of electrostatic theorems,

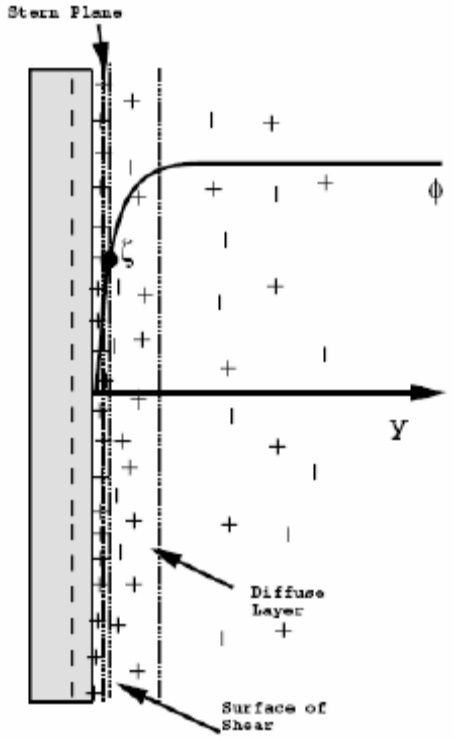

Figure 12. Electric Double layer.

The relation between electric potential Ψ, and net volume charge density ρ_e in each point of fluid, is decrypted by Poisson equation as follows:

$$\frac{\partial^2 \psi}{\partial y^2} + \frac{\partial^2 \psi}{\partial z^2} = -\frac{\rho_e}{\varepsilon_r . \varepsilon_0} \tag{8}$$

ε_r, *and* ε_0 represent the dielectric constant of the solution and permittivity of vacuum respectively. Assuming the Boltzman distribution equation is applicable, the number concentration of the type-i ion in an electrolyte fluid can be considered as follows:

$$n_i = n_{i0}.\exp(\frac{-z_i e\psi}{k_b T}) \tag{9}$$

Where n_{i0} and z_i are the bulk concentration and the valence of type-i ion, respectively, e is the elementary charge, k_b is the Boltzman constant, and T is the absolute temperature. This equation is established only when the system is in equilibrium state. The net volume charge density is commensurate to difference between concentration of cations and anions, via

$$\rho_e = z.e.(n_+ - n_-) = -2zen_0 \sinh(\frac{ze\psi}{k_b T}) \tag{10}$$

Substitution of equation (10) into equation (8) leads to the conspicuous Poisson-Boltzman equation:

$$\frac{\partial^2 \psi}{\partial y^2} + \frac{\partial^2 \psi}{\partial z^2} = \frac{2zen_0}{\varepsilon_r \varepsilon_0} \sinh(\frac{ze\psi}{k_b T}) \tag{11}$$

With considering the Debye-Huckel parameter and following dimensionless groups:

$$\aleph = (\frac{2z^2 e^2 n_0}{\varepsilon_r \varepsilon_0 k_b T})^{1/2} \tag{12}$$

$$D_h = \frac{2H_t W_c}{H_t + W_c} \tag{13}$$

$$Y = \frac{y}{D_h} \tag{14}$$

$$Z = \frac{z}{D_h} \tag{15}$$

$$K = \aleph.D_h \tag{16}$$

$$\Psi = ze\frac{\psi}{k_b T} \tag{17}$$

Where D_h is hydraulic diameter of the rectangular channel, Y and Z are non-dimensional coordinates. By using above non-dimensionless groups equation (11) can be non-dimensionalized as:

$$\frac{\partial^2 \psi}{\partial Y^2} + \frac{\partial^2 \psi}{\partial Z^2} = K^2 \sinh\psi \tag{18}$$

Here K, is the non-dimensional electro-kinetic diameter, depicted as the ratio of the hydraulic diameter to the electrical double layer thickness, and ψ is the non-dimensional electrical potential standing for the ratio of the electrical energy $ze\psi$ to the thermal energy $k_b T$. Considering figure 3 we can issue following boundary conditions:

$$\begin{aligned} &Y=0 \Rightarrow \psi=\bar{\zeta} && Y=\frac{H}{D_h} \Rightarrow \psi=\bar{\zeta} \\ &Z=0 \Rightarrow \frac{\partial \psi}{\partial Z}=0 && Z=\frac{W}{D_h} \Rightarrow \psi=\bar{\zeta} \end{aligned} \tag{19}$$

Where $\bar{\zeta}$ defined by $\bar{\zeta} = \frac{ze\zeta}{k_b T}$ is a non-dimensional zeta potential of the channel walls (here ζ is the potential of the channel wall). The zeta potential is an electric potential at the channel walls. After solving equation (18) and computing ψ, the net volume charge density can be obtained as follows:

$$\rho_e(Y,Z) = -2zen_0 \sinh\psi(Y,Z) \tag{20}$$

This net volume charge density is needed for computing of body forces originating from EDL.

Modified Navier-Stokes Equations

Assuming a laminar fully developed flow in rectangular channels in positive x-direction, the components of velocity satisfy $u = u(y,z)$ and $v = w = 0$ in terms of Cartesian coordinate. The equation of motion is written as follows:

$$\frac{\partial^2 u}{\partial y^2} + \frac{\partial^2 u}{\partial z^2} = \frac{1}{\mu_f}\frac{dP}{dx} - \frac{1}{\mu_f} E_x \rho_e(y,z) \tag{21}$$

In this equation the final term at right hand, is the effects of body forces originating from EDL. Considering following dimensionless groups we can obtain the non-dimensional form of equation (21),

$$\mathrm{Re}_0 = \frac{\rho_f D_h U}{\mu_f} \tag{22}$$

$$\bar{u} = \frac{u}{U} \tag{23}$$

$$\bar{P} = \frac{P - P_0}{\rho_f U^2} \tag{24}$$

$$\bar{X} = \frac{x}{D_h \operatorname{Re}_0} \tag{25}$$

$$\frac{d\bar{P}}{d\bar{X}} = \frac{D_h \operatorname{Re}_0}{\rho_f U^2} \frac{dP}{dx} \tag{26}$$

$$\bar{E}_x = \frac{E_x D_h \operatorname{Re}_0}{\zeta_0} \tag{27}$$

$$\bar{G}_1 = \frac{2zn_0\zeta_0}{\rho_f U^2} \tag{28}$$

Substitution of resent equations in equation (21), the non-dimensional for of this equation can be obtained:

$$\frac{\partial^2 \bar{u}}{\partial Y^2} + \frac{\partial^2 \bar{u}}{\partial Z^2} = \frac{d\bar{P}}{d\bar{X}} + \bar{G}_1 \bar{E}_x \sinh \Psi(Y, Z) \tag{29}$$

Related boundary conditions are as follows:

$$\begin{aligned} &Y = 0 \;\Rightarrow\; \bar{u} = 0 && Y = \frac{H_c}{D_h} \;\Rightarrow\; \bar{u} = 0 \\ &z = 0 \;\Rightarrow\; \frac{\partial \bar{u}}{\partial z} = 0 && Z = \frac{W_c}{D_h} \;\Rightarrow\; \bar{u} = 0 \end{aligned} \tag{30}$$

After numerical solution of equation (29) the velocity field will be obtained.

Energy Equation

As presented in figure 1, a silicon wafer plate with a large number of microchannels is connected to the chip. A liquid is forced to flow through these microchannels to remove the heat. All microchannels are assumed to have a uniform rectangular cross-section with geometric parameters as shown in table 2. For a steady-state, fully developed, laminar flow in a microchannel, the energy equation (with consideration of the axial thermal conduction in flow direction and the viscous dissipation) for the cooling liquid takes the specific form:

$$u\frac{\partial\theta}{\partial x}=\alpha_f\left(\frac{\partial^2\theta}{\partial x^2}+\frac{\partial^2\theta}{\partial y^2}+\frac{\partial^2\theta}{\partial z^2}\right)+\frac{\mu_f}{\rho_f C_{pf}}\left[\left(\frac{\partial u}{\partial y}\right)^2+\left(\frac{\partial u}{\partial z}\right)^2\right] \tag{31}$$

Where θ and α_f are the temperature and the thermal diffusivity of the cooling liquid, respectively, C_{pf} is the specified heat capacity of the cooling liquid. Based on presented computational domain, the adiabatic condition can be used along the channel symmetric center line:

$$z=0 \quad \Rightarrow \quad \frac{\partial\theta}{\partial z}=0 \tag{32}$$

At the bottom of channels, a uniform heat flux of q" is imposed over the heat sink, and can be expressed as:

$$y=0 \quad \Rightarrow \quad q''=-k_f\left(\frac{\partial\theta}{\partial y}\right) \tag{33}$$

Hear k_f is the thermal conductivity of the liquid coolant. Since the thermal conductivity of the glass is about two-order of magnitude lower than that the top boundary is insulted. This is a conservative assumption which will lead to slight underestimation of the overall heat transfer coefficient. This assumption yields:

$$y=H \quad \Rightarrow \quad \frac{\partial\theta}{\partial y}=0 \tag{34}$$

Numerical Solution

The power-low scheme is used to model the combined convection-diffusion effects in the transport equations with FVM approach. The SIMPLER scheme is employed to resolve the pressure-velocity coupling. The resulting algebraic equations are solved using a line-by-line Tri-Diagonal matrix Algorithm.

The study cases are the same given in table (2) and the computed results were compared in table (7) with the results of Toh et. al. (2002) (without EDL), and the experimental results of Tuckermann (1984). The thermal resistance was the basis of their comparisons. It is shown that sufficiently reasonable agreement exists in such comparison. The thermal resistance because of decreasing in volumetric flow rate and consequently increasing in $T_{\max}$ increases from case 1 to case 4.

Table 7. Thermal resistance comparison

Case	Heat Flux (w/m^2) ×10-4	104× (m^2K/W)Thermal Resistance		
		Tuckerman's Result	Toh's Result	Current numerical Result
1	36.4	0.280	0.253	0.301
2	181	0.110	0.157	0.136
3	277	0.113	0.128	0.116
4	790	0.090	0.105	0.086

For considering of effects of EDL, the gradient of pressure, velocity profile, and temperature profile are inspected for both, existing of EDL with two amounts for zeta potential, 75 milivolt and 200 milivolt, and absence of EDL. The 75 milivolt zeta potential is considered for feeble EDL effects, and 200 milivolt zeta potential is selected for strong EDL effects. The effects of EDL on distribution of pressure along the microchannel are showed in figure 13 for case1.

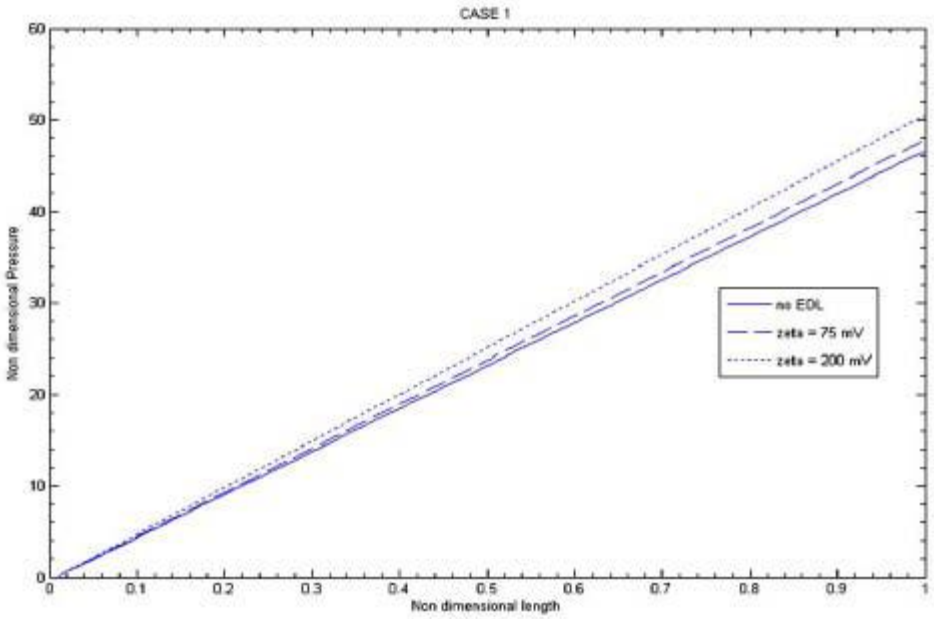

Figure 13. variation of dimensionless pressure drop with respect to dimensionless length of channel.

The percentage of effects of EDL on dimensionless distribution of pressure for case 1 to case 4 is presented in table (7).

Table 7. The percentage of variation of dimensionless distribution of pressure

Case	The percentage of variation of dimensionless distribution affected by EDL	
	Zeta Potential (75mv)	Zeta Potential (200mv)
0	9.4	24.7
1	2.6	8.5
2	4.1	10.2
3	4.4	10.9
4	6.2	13.7

The illustrated difference in alterations of pressure affected of EDL is because of coming into existence of apparent viscosity that is much more than viscosity in absence of EDL. As it can be seen in table (7), the percentage of alterations of pressure in 75 milivolt zeta potential for cases 1-4 is not so intense, but in 200 milivolt zeta potential for case 0 that has minimum channel width, exists a large mutation causes to considerable thickness of EDL with respect to channel width. Hence we can conclude that whit increasing of thickness of EDL in comparison with channel width the effects of EDL will be stronger. Pressure drop considerations will determine the required pumping power. The more pressure drop, the more required pumping power. Thus, with existing of a powerful EDL effect, we will require much pumping power, and this is not so suitable. The effects of EDL on velocity profile are depicted in figures 14 and 15 for case 0, and case 1 respectively, and percentage of alterations of velocity for cases 1-4 is shown in table (8). As presented in table (8), a large mutation in velocity alliteration exists for case 0 in 200 milivolt zeta potential as there is for pressure alliteration in this case. Adhesiveness of ions to channels walls and body forces originated from EDL causes to reducing of volumetric flow rate. Decreasing in characteristic length of microchannel, and increasing in body forces originating from EDL causes to increasing in velocity alliteration.

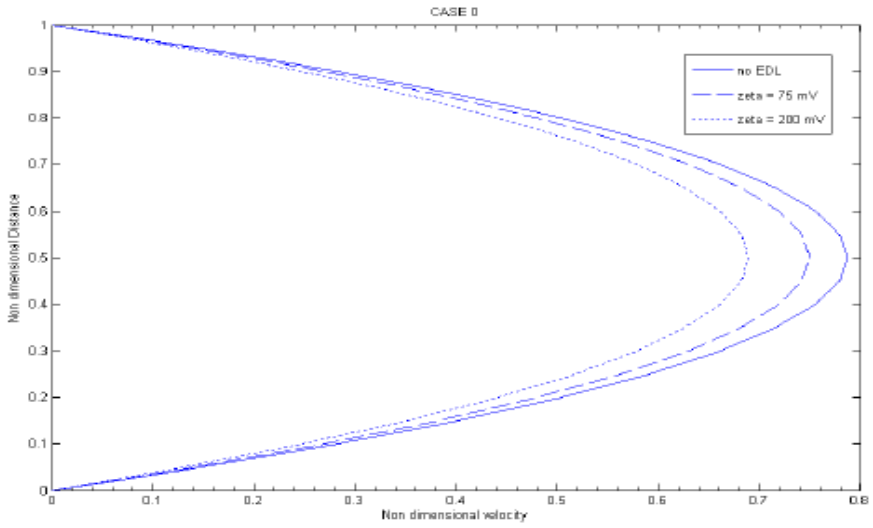

Figure 14. Variation of dimensionless velocity profile with respect to dimensionless thickness of channel for case 0.

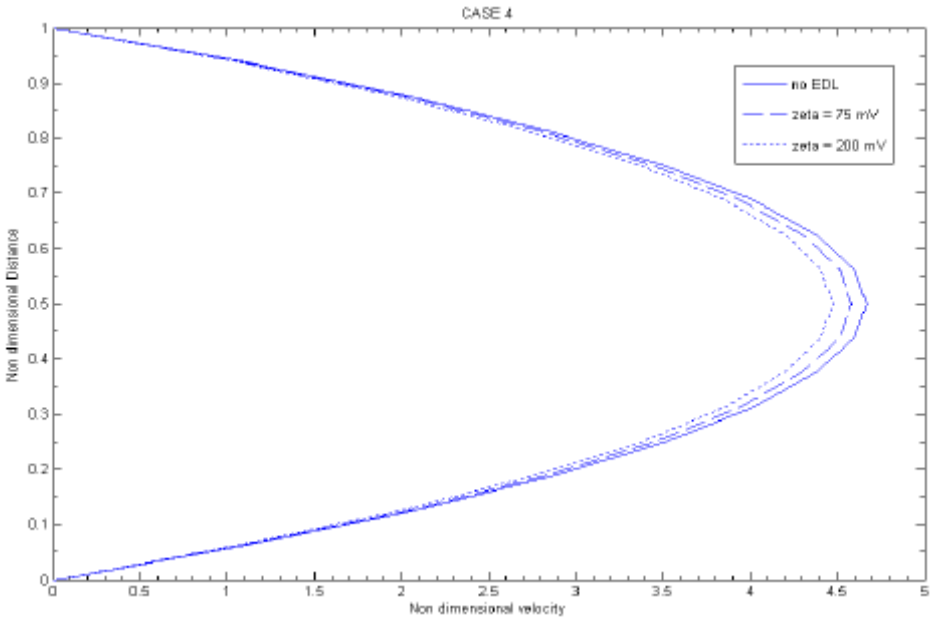

Figure 15. Variation of dimensionless velocity profile with respect to dimensionless thickness of channel for case 4.

Table 8. The percentage of variation of dimensionless velocity

Case	The percentage of variation of dimensionless Velocity affected by EDL	
	Zeta Potential (75mv)	Zeta Potential (200mv)
0	4.8	12.5
1	0.9	2.1
2	1.4	3.1
3	1.6	3.5
4	2.9	4.1

The EDL effects on dimensionless temperature profile with respect to dimensionless channel high are presented for cases 3, 4 in figures 16 and 17. Asshown, temperature of cooling fluid decreases from bottom wall that is exposed to uniform heat flux to top of the channel that is adiabatic.The gradient of temperature near the upper wall of the channel depicted that there is no heat flux near the wall. The effects of EDL on dimensionless temperature profile is shown for cases 0-4 in table (9) on percentage base. As it is obvious, the presence of EDL causes an augment of temperature, particularly in case 0, this growth is result of reduction in volumetric flow rate. The growth of temperature of causes the reduction in Nusselt number.

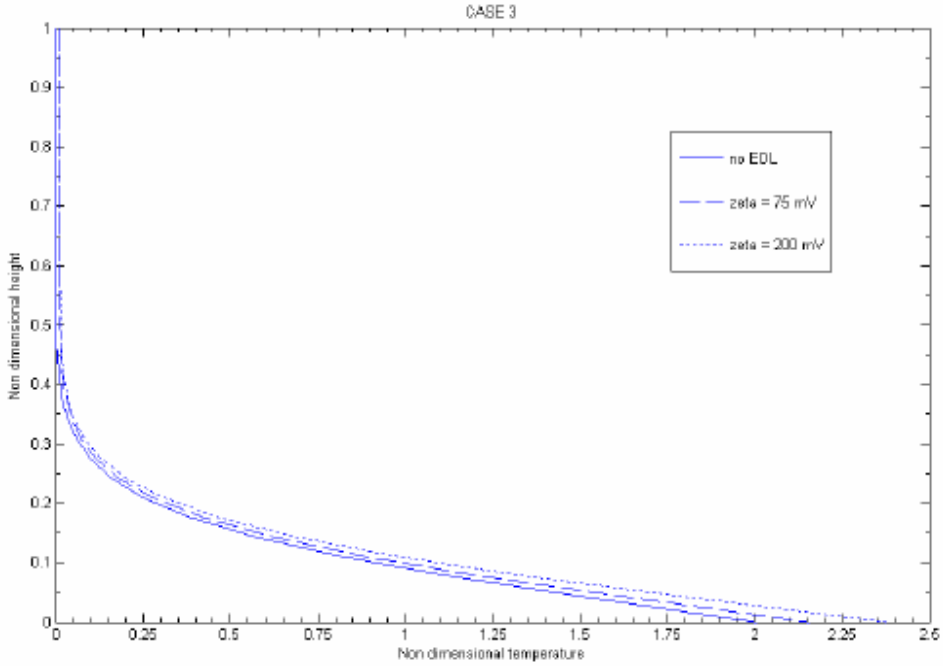

Figure 16. variation of dimensionless Temperature profile with respect to dimensionless height of channel for case 3.

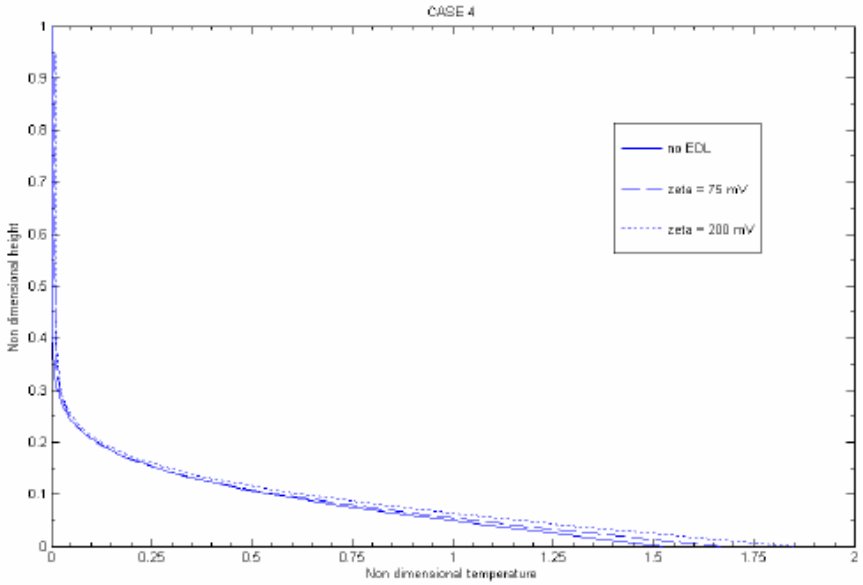

Figure 17. variation of dimensionless Temperature profile with respect to dimensionless height of channel for case 4.

Table 9. The percentage of variation of dimensionless Temperature

Case	The percentage of variation of dimensionless Temperature affected by EDL	
	Zeta Potential (75mv)	Zeta Potential (200mv)
0	8/8	26/6
1	3/9	9/8
2	4/7	12/6
3	5/1	13/1
4	6/4	14/8

We can say that; considering the effects of EDL is very necessary for exact solution of equations of motion in electrolyte fluid flow. Because of using of ionized liquid in practical manners, the effects of EDL are not negligible. For the cases that characteristic length of microchannel is comparable with the thickness of EDL or exist a high electric potential, the liquid flow and heat transfer characteristics are significantly affected by the presence of the EDL, and omission of the effects of EDL causes to a much deviates from the prediction of conventional theorems. Presence of EDL causes to an apparent viscosity that is much more than the viscosity of fluid, and increasing of zeta potential also causes to decreasing in volumetric flow rate. Similarly, presence of EDL leading to a large amount of pressure drop in microchannel heat sinks. As a result we can say that, existence of EDL causes to decreasing in efficiency of microchannel.

3. POROUS MICRO-STRUCTURE APPROACH

As proposed by Kim and Kim (1999), the MCHS can be modeled as a porous micro-structure. That is, the region between the cover plate and base plate(substructure) of the MCHS is modeled as a porous medium (figure 2). The governing equations for the fluid flow and heat transfer can be established by applying the volume-averaged technique. Since the one equation model is valid only when the fluid phase is in local equilibrium with the solid phase and is not suitable in the evaluation of MCHS thermal performance (Tsai and Chen, 2007), the two-equation model is employed. The governing equations for the fluid and energy transport under fully hydrodynamic and thermal development conditions can be written as

Fluid flow:

$$-\frac{dp_f}{dx}+\mu\frac{d^2\tilde{u}}{dy^2}-\frac{\mu}{K}\varepsilon\tilde{u}-\rho_f C\tilde{u}^2=0 \tag{35}$$

Energy in solid phase:

$$k_{se}\frac{\partial^2 T_s}{\partial y^2}=ha(T_s-\tilde{T}_f) \tag{36}$$

Energy in fluid phase:

$$\varepsilon(\rho c_p)_f u\frac{\partial \tilde{T}_f}{\partial x} = ha(T_s - \tilde{T}_f) + \frac{\partial}{\partial y}(k_{fe}\frac{\partial \tilde{T}_f}{\partial y}) \tag{37}$$

In which the k_{se} and k_{fe} are defined as following

$$k_{se} = (1-\varepsilon)k_s \tag{39}$$

$$k_{fe} = \varepsilon k_f \tag{40}$$

In equations (35)–(37), p, $\tilde{u}$, $\tilde{T}_f$, T_s, C and h are the volume-averaged fluid pressure, fluid velocity, fluid temperature, solid temperature, inertia force and interfacial heat transfer coefficient between fluid and solid, respectively. The MCHS shown in figure 1, modeled as a porous medium, the porosity ε, permeability K and wetted area per volume a can be expressed as (Bejan, 1984).]

$$\varepsilon = \frac{w_c}{w_c + (H_t - H_c)},\ a = \frac{2}{w_c + (H_t - H_c)} \tag{41}$$

The boundary conditions for this problem are:

$$\tilde{u} = 0 \text{ at } y = 0, H \tag{42-a}$$

$$\tilde{T}_f = T_s = T_w \text{ at } y = 0 \tag{42-b}$$

$$\frac{\partial T_s}{\partial y} = \frac{\partial \tilde{T}_f}{\partial y} = 0 \text{ at } y = H \tag{42-c}$$

To solve the governing equations (35)–(37), the permeability K and the interstitial heat transfer coefficient h should be determined in advance. For the present configuration, these parameters can be determined analytically through an approximation method proposed by Kim(2004). It is assumed that the characteristics of pressure drop across and heat transfer from the fins under consideration can be approximated as those found for the Poiseuille flow between two infinite parallel plates that are subject to a constant heat flux. Then the velocity and temperature distributions can be obtained easily as:

$$\tilde{u} = \frac{w^2{}_c}{2\mu}(-\frac{dp}{dx})[(\frac{z}{w_c}) - (\frac{z}{w_c})^2] \tag{43}$$

$$\tilde{\tilde{T}}_f = \frac{qw_c}{k_f}[-(\frac{z}{w_c})^4 + 2(\frac{z}{w_c})^3 - (\frac{z}{w_c})] + T_w \tag{44}$$

$$\tilde{u} = \frac{1}{V_f}\int_{V_f} u dV = \frac{{w_c}^2}{12\mu}(-\frac{dp}{dx}) \tag{45}$$

$$\tilde{\tilde{T}}_f = \frac{1}{V_f}\int_{V_f} T_f dV = T_w - \frac{{w_c}^2}{10\alpha}\tilde{u}\frac{d\overline{T}_f}{dx} \tag{46}$$

In which the α is the aspect ratio of the channels.

CONCLUSION

New developments on heat transfer and fluid flow computational techniques in different types of microchannel heat sinks was investigated. The numerical results of temperature distribution, thermal resistances and pressure drop were shown and the results had good consistency with experimental data.

REFERENCES

[1] Tsai, T., and Chein, R. (2007). Performance analysis of nanofluid-cooled microchannel heat sinks. *Int. J. Heat and Fluid Flow*, In press.

[2] Tuckerman, D.B. and Pease, R.F. (1981). High-performance heat sinking for VLSI. *IEEE Electronic Devices Letters EDL*, Vol. 2, pp. 126–129.

[3] Knight, R.W., Hall, D.J., Goodling, J.S., Jaeger, R.C. (1992). Heat sink optimization with application to microchannels. *IEEE Transactions on Components, Hybrids, and Manufacturing Technology*, Vol. 15, pp. 832–842.

[4] Ambatipudi, K.K., Rahman, M.M. (2000). Analysis of conjugate heat transfer in microchannel heat sinks. *Numerical Heat Transfer Part A, Vol.* 37, pp.711–731.

[5] Fedorov, A.G., Viskanta, R. (2000). Three-dimensional conjugate heat transfer in the microchannel heat sink for electronic packaging. *International Journal of Heat and Mass Transfer*, Vol. 43, pp.399–415.

[6] Lee, P., Garimella, S.V., Liu, D. (2005). Investigation of heat transfer in rectangular microchannels. *International Journal of Heat and Mass Transfer Vol*. 48, pp.1688–1704.

[7] Li, J., Peterson, G.P., Cheng, P. (2004). Three-dimensional analysis of heat transfer in a micro-heat sink with single phase flow. *Int. J. of Heat and Mass Transfer*, Vol. 47, pp.4215–4231.

[8] Li, J. and Peterson, G.P. (2006). Geometric optimization of a micro heat sink with liquid flow. *IEEE Transactions on Components and Packaging Technologies*, Vol. 29, pp.145–154.

[9] Amanifard, N. and Haghi, A. K. (2006). Numerical Investigation of fluid flow and heat transfer in microchannels. *Int. J. Heat and Technology,* Vol.1, pp…….

[10] Amanifard,N. Borji, M., Haghi, A. K. (2007). Heat Transfer in Porous Media. *Brazilian J. Chemical Engineering,* Vol.1, In press.

[11] Amanifard,N. and Haghi, A. K. (2007). Numerical Investigation of fluid flow and heat transfer in microchannels. *Int. J. Heat and Technology,* Vol.1, In press.

[12] Qu, W., Mudawar, I. (2002). Experimental and numerical study of pressure drop and heat transfer in a single-phase microchannel heat sink. *Int. J. of Heat and Mass Transfer,* Vol. 45, pp. 2549–2565.

[13] Tiselj, I., Hetsroni, G., Mavko, B., Mosyak, A., Pogrebnyak, E., Segal, Z. (2004). Effect of axial conduction on the heat transfer in microchannels. *Int. J. of Heat and Mass Transfer,* Vol.47, pp. 2551–2565.

[14] Lu, T. J. (1999). Heat transfer efficiency of metal honeycombs. *Int. J. Heat 7 Mass Transfer,* Vol.42, pp.2031-2040.

[15] Gu, T. J. and Lu, A. G., Evans. (2001). On the design of two dimensional cellar metals for combined heat dissipation and structural load capacity. *Int. J. Heat and Mass Transfer,* Vol. 44, pp. 2163-2175.

[16] Kohn, J.C.Y. and Colony, R. (1986). Heat transfer of microstructures for integrated circuits. *Int. J. Heat and Mass Transfer,* Vol. 13, pp. 89-98.

[17] Tien, C.L. and Kuo, S.M. (1987). Analysis of forced convection in microstructures for electronic system cooling. *Proceeding of Int. Symp. Cooling Technology for Electronic Equipment, Honolulu, HI*, pp. 217-226.

[18] Kim, S.J., Kim, D. (1999). Forced convection in microstructures for electronic equipment cooling. *ASME Journal of Heat Transfer*. 121, pp. 639–645.

[19] Knight, R.W., Hall, D.J., Goodling, J.S., Jaeger, R.C. (1992). Heat sink optimization with application to microchannels. *IEEE Transactions on Components, Hybrids, and Manufacturing Technology*. 15, pp. 832–842.

[20] Zhao, C.Y., Lu, T.J. (2002). Analysis of microchannel heat sinks for electronics cooling. *International Journal of Heat and Mass Transfer*. 45, pp. 4857–4869.

[21] Vafai, K. and Tien, C. L. (1981). Boundary and inertia effects on flow and heat transfer in porous media. *Int. J. Heat and Mass Transfer.* 43, pp. 195-203.

[22] Wu, P.Y. and Little, W.A. (1983). Measurement of friction factor for flow of gases in very fine channels used for microminiature, *Joule Thompson refrigerators,Cryogenics.* 24 (8), pp.273-277.

[23] Choi, S.B., Barren, R.R., Warrington, R.O. (1991). Fluid Flow and Heat Transfer in Microtubes. *ASME DSC.* 40 pp.89-93.

[24] Adams, T.M., Abdel-Khalik, S.I., Jeter, S.M., Qureshi, Z. H. (1998). AN Experimental investigation of single-Phase Forced Convection in Microchannels. *Int. J. Heat Mass Transfer.* 41 pp. 851-857.

[25] Peng, X.F., Peterson, G.P. (1996). Convective Heat Transfer and Flow Friction for Water Flow in Microchannel Structure. *Int. J. Heat Mass Transfer*. 36, pp. 2599-2608.

[26] Mala, G., Li, D., Dale, J.D. (1996). Heat Transfer and Fluid Flow in Microchannels. *J. Heat Transfer,* 40 pp.3079-3088.

[27] Tuckerman, D.B. (1984). Heat transfer microstructures for integrated circuits. Ph.D. thesis, Stanford University.

[28] Toh, K.C., Chen, X.Y., and Chai, J.C. (2002). Numerical Computation of Fluid Flow and Heat Transfer in Microchannels. *Int. J. Heat and Mass Transfer*. 45, pp. 5133–5141.

[29] Kim, S.J. (2004).Methods for thermal optimization of microchannel heat sinks. *Heat Transfer Eng.* 25, pp.37–49.

In: Monomers, Oligomers, Polymers, Composites… ISBN: 978-1-60456-877-6
Editors: R. A. Pethrick, G.E. Zaikov et al.

Chapter 11

IMAGE ANALYSIS OF PORE SIZE DISTRIBUTION IN ELECTROSPUN NANOFIBER WEBS: NEW TRENDS AND DEVELOPMENTS

M. Ziabari, V. Mottaghitalab and A. K. Haghi*
The University of Guilan, P. O. Box 3756, Rasht, Iran

ABSTRACT

Nanofibers produced by electrospinning method are widely used for drug delivery, as tissue scaffolding materials and filtration purposes where specific pore characteristics are required. For continued growth in these areas, it is critical that the nanofibers be properly designed for these applications to prevent failure. Most of the current methods only provide an indirect way of determining pore structure parameters and contain inherent disadvantages. In this study, we developed a novel image analysis method for measuring pore characteristics of electrospun nanofiber webs. 5 electrospun webs with different pore characteristics were analyzed by this method. The method is direct, so fast and presents valuable and comprehensive information regarding to pore structure parameters of the webs. Two sets of simulated images were generated to study the effects of web density, fiber diameter and its variations on pore characteristics. The results indicated that web density and fiber diameter significantly influence the pore characteristics whereas the effect of fiber diameter variations was insignificant.

1. INTRODUCTION

Fibers with a diameter of around 100 nm are generally classified as *nanofibers*. What makes nanofibers of great interest is their extremely small size. Nanofibers compared to conventional fibers, with higher surface area to volume ratios and smaller pore size, offer an opportunity for use in a wide variety of applications. To date, the most successful method of producing nanofibers is through the process of *electrospinning*. The electrospinning process

* Corresponding author E-Mail: Haghi@Guilan.ac.ir

uses high voltage to create an electric field between a droplet of polymer solution at the tip of a needle and a collector plate. When the electrostatic force overcomes the surface tension of the drop, a charged, continuous jet of polymer solution is ejected. As the solution moves away from the needle and toward the collector, the solvent evaporates and jet rapidly thins and dries. On the surface of the collector, a nonwoven web of randomly oriented solid nanofibers is deposited [1]-[5]. Figure 1 illustrates the electrospinning setup.

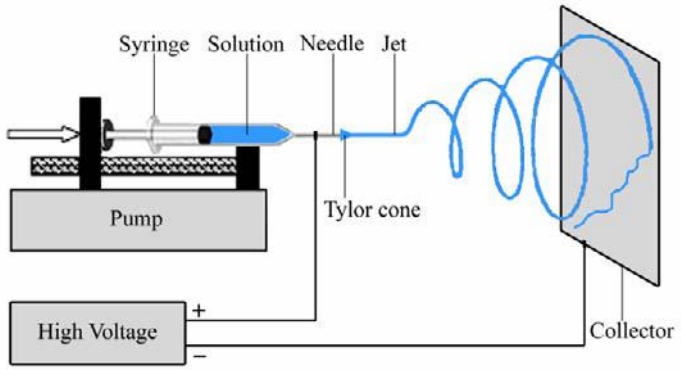

Figure 1. Electrospinning setup.

Material properties such as melting temperature and glass transition temperature as well as structural characteristics of nanofiber webs such as fiber diameter distribution, pore size distribution and fiber orientation distribution determine the physical and mechanical properties of the webs. The surface of electrospun fibers is important when considering end-use applications. For example, the ability to introduce porous surface features of a known size is required if nanoparticles need to be deposited on the surface of the fiber, if drug molecules are to be incorporated for controlled release, as tissue scaffolding materials and for acting as a cradle for enzymes [6]. Besides, filtration performance of nanofibers is strongly related to their pore structure parameters, i.e., percent open area (POA) and pore-opening size distribution (PSD). Hence, the control of the pore of electrospun webs is of prime importance for the nanofibers that are being produced for these purposes. There is no literature available about the pore size and its distribution of electrospun fibers and in this work, the pore size and its distribution was measured using an image analysis technique.

Current methods for determining PSD are mostly indirect and contain inherent disadvantages. Recent technological advancements in image analysis offer great potential for a more accurate and direct way of determining the PSD of electrospun webs. Overall, the image analysis method provides a unique and accurate method that can measure pore opening sizes in electrospun nanofiber webs.

2. METHODOLOGY

The porosity, ε_V, is defined as the percentage of the volume of the voids, V_v, to the total volume (voids plus constituent material), V_t, and is given by

$$\varepsilon_V = \frac{V_v}{V_t} \times 100$$

Similarly, the Percent Open Area (POA), ε_A, that is defined as the percentage of the open area, A_o, to the total area A_t, is given by

$$\varepsilon_A = \frac{A_o}{A_t} \times 100$$

Usually porosity is determined for materials with a three-dimensional structure, e.g. relatively thick nonwoven fabrics. Nevertheless, for two-dimensional textiles such as woven fabrics and relatively thin nonwovens it is often assumed that porosity and POA are equal [7].

The size of an individual opening can be defined as the surface area of the opening, although it is mostly indicated with a diameter called Equivalent Opening Size (EOS). EOS is not a single value, for each opening may differ. The common used term in this case is the diameter, O_i, corresponding with the equivalent circular area, A_i, of the opening.

$$O_i = (4A_i / \pi)^{1/2}$$

This diameter is greater than the side dimension of a square opening. A spherical particle with that diameter will never pass the opening (Figurea) and may therefore not be considered as an equivalent dimension or equivalent diameter. This will only be possible if the diameter corresponds with the side of the square area (Figureb). However, not all openings are squares, yet the equivalent square area of openings is used to determine their equivalent dimension because this simplified assumption results in one single opening size from the open area. It is the diameter of a spherical particle that can pass the equivalent square opening, hence the equivalent opening or pore size, O_i, results from

$$O_i = (A_i)^{1/2}$$

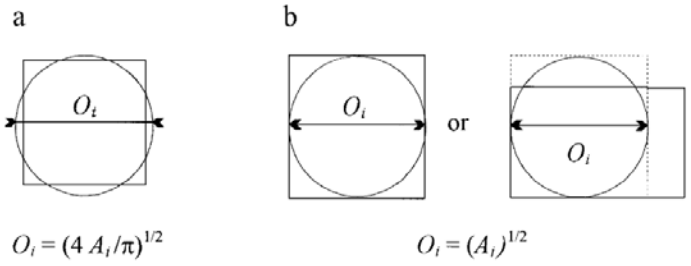

Figure 2. Equivalent opening size, O_i, based on (a) equivalent area, (b) equivalent size.

From the EOSs, Pore Size Distribution (PSD) and an equivalent diameter for which a certain percentage of the opening have a smaller diameter (O_x, pore opening size that x percent of pores are smaller than that size) may be measured.

The PSD curves can be used to determine the uniformity coefficient, C_u, of the investigated materials. The uniformity coefficient is a measure for the uniformity of the openings and is given by

$$C_u = O_{60}/O_{10}$$

The ratio equals 1 for uniform openings and increases with decreasing uniformity of the openings [7].

Pore characteristic is one of the main tools for evaluating the performance of any nonwoven fabric and for electrospun webs as well. Understanding the link between processing parameters and pore structure parameters will allow for better control over the properties of electrospun fibers. Therefore there is a need for the design of nanofibers to meet specific application needs. Various techniques may be used to evaluate pore characteristics of porous materials including sieving techniques (dry, wet and hydrodynamic sieving), mercury porosimetry and flow porosimetry (bubble point method) [8], [9]. As one goes about selecting a suitable technique for characterization, the associated virtues and pitfalls of each technique should be examined. The most attractive option is a single technique which is non-destructive, yet capable of providing a comprehensive set of data [10].

2.1. Sieving Methods

In dry sieving, glass bead fractions (from finer to coarser) are sieved through the porous material. In theory, most of the glass beads from the first glass bead fraction should pass. As larger and larger glass bead fractions are sieved, more and more glass beads should become trapped within and on top of the material. The number of pores of a certain size should be reflected by the percentage of glass beads passing through the porous material during each glass bead fraction sieved; however, electrostatic effects between glass beads and between glass beads and the material can affect the results. Glass beads may stick to fibers making the pores effectively smaller and they may also agglomerate to form one large glass bead that is too large to pass through the any of the pores. Glass beads may also break from hitting each other and the sides of the container, resulting in smaller particles that can pass through smaller openings.

In hydrodynamic sieving, a glass bead mixture is sieved through a porous material under alternating water flow conditions. The use of glass bead mixtures leads to results that reflect the original glass bead mixture used. Therefore, this method is only useful for evaluating the large pore openings such as O_{95}. Another problem occurs when particles of many sizes interact, which likely results in particle blocking and bridge formation. This is especially a problem in hydrodynamic sieving because the larger glass bead particles will settle first when water is drained during the test. When this occurs, fine glass beads which are smaller than the pores are prevented from passing through by the coarser particles.

In wet sieving, a glass bead mixture is sieved through a porous material aided by a water spray. The same basic mechanisms that occur when using the hydrodynamic sieving method also take place when using the wet sieving method. Bridge formation is not as pronounced in

the wet sieving method as in the hydrodynamic sieving method; however, particle blocking and glass bead agglomeration are more pronounced [8], [9].

The sieving tests are very time-consuming. Generally 2 hours are required to perform a test. The sieving tests are far from providing a complete PSD curve because the accuracy of the tests for pore sizes smaller than 90 μm is questionable [12].

2.2. Mercury Porosimetry

Mercury porosimetry is a well known method which is often used to study porous materials. This technique is based on the fact that mercury as a non-wetting liquid does not intrude into pore spaces except under applying sufficient pressure. Therefore, a relationship can be found between the size of pores and the pressure applied.

In this method, a porous material is completely surrounded by mercury and pressure is applied to force the mercury into pores. As mercury pressure increases the large pores are filled with mercury first. Pore sizes are calculated as the mercury pressure increases. At higher pressures, mercury intrudes into the fine pores and when the pressure reaches a maximum, total open pore volume and porosity are calculated.

The mercury porosimetry thus gives a PSD based on total pore volume and gives no information regarding the number of pores of a porous material. Pore sizes ranging from 0.0018 to 400 μm can be studied using mercury porosimetry. Pore sizes smaller than 0.0018 μm are not intruded with mercury and this is a source of error for porosity and PSD calculations. Furthermore, mercury porosimetry does not account for closed pores as mercury does not intrude into them. Due to applying high pressures, sample collapse and compression is possible, hence it is not suitable for fragile compressible materials such as nanofiber sheets. Other concerns would include the fact that it is assumed that the pores are cylindrical, which is not the case in reality. After the mercury intrusion test, sample decontamination at specialized facilities is required as the highly toxic mercury is trapped within the pores. Therefore this dangerous and destructive test can only be performed in well-equipped labs [6], [8], [9].

2.3. Flow Porosimetry (Bubble Point Method)

The flow porosimetry is based on the principle that a porous material will only allow a fluid to pass when the pressure applied exceeds the capillary attraction of the fluid in largest pore. In this test, the specimen is saturated with a liquid and continuous air flow is used to remove liquid from the pores. At a critical pressure, the first bubble will come through the largest pore in the wetted specimen. As the pressure increases, the pores are emptied of liquid in order from largest to smallest and the flow rate is measured. PSD, number of pores and porosity can be derived once the flow rate and the applied pressure are known. Flow porosimetry is capable of measuring pore sizes within the range of 0.013–500 μm.

As the air only passes through the through pores, characteristics of these pores are measured while those of closed and blind pores are omitted. Many times, 100% total flow is not reached. This is due to porewick evaporation from the pores when the flow rate is too high. Extreme care is required to ensure the air flow does not disrupt the pore structure of the

specimen. The flow porosimetry method is also based on the assumption that the pores are cylindrical, which is not the case in reality. Finding a liquid with low surface tension which could cover all the pores, has no interaction with the material and does not cause swelling in material is not easy all the times and sometimes is impossible [6], [8], [9].

2.4. Image Analysis

Because of its convenience to detect individual pores in a nonwoven image, it seemed to be advantageous to use image analysis techniques for pore measurement. Image analysis was used to measure pore characteristics of woven [11] and nonwoven geotextiles [12]. In the former, successive *erosion* operations with increasing size of *structuring element* was used to count the pore openings larger than a given structuring element. The main purpose of the erosion was to simulate the conditions in the sieving methods. In this method, the voids connected to border of the image which are not complete pores are considered in measurement. Performing opening and then closing operations proceeding pore measurement cause the pore sizes and shapes deviate from the real ones. The method is suitable for measuring pore sizes of woven geotextiles with fairly uniform pore sizes and shapes and is not appropriate for electrospun nanofiber webs of different pore sizes.

In the later case, cross sectional image of nonwoven geotextile was used to calculate the pore structure parameters. A *slicing* algorithm based on a series of morphological operations for determining the mean fiber thickness and the optimal position of the uniform slicing grid was developed. After recognition of the fibers and pores in the slice, the pore opening size distribution of the cross sectional image may be determined. The method is useful for measuring pore characteristics of relatively thick nonwovens and cannot be applied to electrospun nanofiber webs due to extremely small size.

Therefore, there is a need for developing an algorithm suitable for measuring the pore structure parameters in electrospun webs. In response to this need, we have developed a new image analysis based method and presented in the following.

In this method, a binary image of the web is used as an input. First of all, voids connected to the image border are identified and cleared using *morphological reconstruction* [13] where mask image is the input image and marker image is zero everywhere except along the border. Total area which is the number of pixels in the image is measured. Then the pores are labeled and each considered as an object. Here the number of pores may be obtained. In the next step, the number of pixels of each object as the area of that object is measured. Having the area of pores, the porosity and EOS regarding to each pore may be calculated. The data in pixels may then be converted to *nm*. Finally PSD curve is plotted and O_{50}, O_{95} and C_u are determined.

2.4.1. Real Webs

In order to measure pore characteristics of electrospun nanofibers using image analysis, images of the webs are required. These images called micrographs usually are obtained by Scanning Electron Microscope (SEM), Transmission Electron Microscope (TEM) or Atomic Force Microscope (AFM). The images must be of high-quality and taken under appropriate magnifications.

The image analysis method for measuring pore characteristics requires the initial segmentation of the micrographs in order to produce binary images. This is a critical step

because the segmentation affects the results dramatically. The typical way of producing a binary image from a grayscale image is by *global thresholding* [13]] where a single constant threshold is applied to segment the image. All pixels up to and equal to the threshold belong to object and the remaining belong to the background. One simple way to choose the threshold is picking different thresholds until one is found that produces a good result as judged by the observer. Global thresholding is very sensitive to any inhomogeneities in the gray-level distributions of object and background pixels. In order to eliminate the effect of inhomogeneities, *local thresholding* scheme [13]] could be used. In this approach, the image is divided into subimages where the inhomogeneities are negligible. Then optimal thresholds are found for each subimage. A common practice in this case, which is used in this study, is to preprocess the image to compensate for the illumination problems and then apply a global thresholding to the preprocessed image. It can be shown that this process is equivalent to segment the image with locally varying thresholds. In order to automatically select the appropriate thresholds, *Otsu's method* [14]] is employed. This method chooses the threshold to minimize interaclass variance of the black and white pixels. As it is shown in Figure 7, global thresholding resulted in some broken fiber segments. This problem was solved using local thresholding. Note that, since the process is extremely sensitive to noise contained in the image, before the segmentation, a procedure to clean the noise and enhance the contrast of the image is necessary.

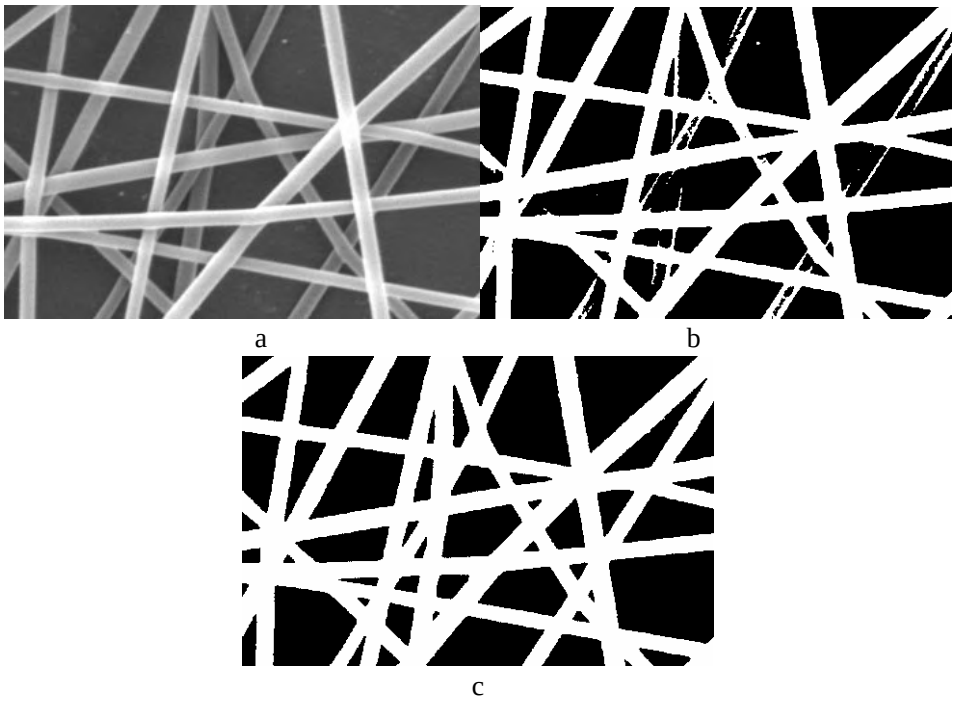

Figure 3. a) A real web, b) Global thresholding, c) Local thresholding.

2.4.2. Simulated Webs

In is known that the pore characteristics of nonwoven webs are influenced by web properties and so are those of electrospun webs. There are no reliable models available for

predicting these characteristics as a function of web properties [15]. In order to explore the effects of some parameters on pore characteristics of electrospun nanofibers, simulated webs are generated. These webs are images simulated by straight lines. There are three widely used methods for generating random network of lines. These are called S-randomness, μ-randomness (suitable for generating a web of continuous filaments) and I-randomness (suitable for generating a web of staple fibers). These methods have been described in details by Abdel-Ghani et al. [16] and Pourdeyhimi et al. [17]. In this study, we used *μ-randomness* procedure for generating simulated images. Under this scheme, a line with a specified thickness is defined by the perpendicular distance *d* from a fixed reference point *O* located in the center of the image and the angular position of the perpendicular *α*. Distance *d* is limited to the diagonal of the image. Figure 2 demonstrates this procedure.

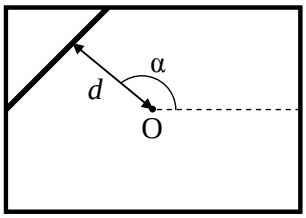

Figure 4. Procedure for μ-randomness.

One of the most important features of simulation is that it allows several structural characteristics to be taken into consideration with the simulation parameters. These parameters are: web density (controlled as line density), angular density (sampled from a normal or random distribution), distance from the reference point (sampled from a random distribution), line thickness (sampled from a normal distribution) and image size.

3. EXPERIMENTAL

Nanofiber webs were obtained from electrospinning of PVA with average molecular weight of 72000 g/mol (MERCK) at different processing parameters for attaining different pore characteristics. Table 1summarizes the electrospinning parameters used for preparing the webs. The micrographs of the webs were obtained using Philips (XL-30) environmental Scanning Electron Microscope (SEM) under magnification of 10000X after being gold coated. Figure 8 shows the micrographs of the electrospun webs.

Table 1. Electrospinning parameters used for preparing nanofiber webs

No.	Concentration (%)	Spinning Distance (Cm)	Voltage (KV)	Flow Rate (ml/h)
1	8	15	20	0.4
2	12	20	15	0.2
3	8	15	20	0.2
4	8	10	15	0.3
5	10	10	15	0.2

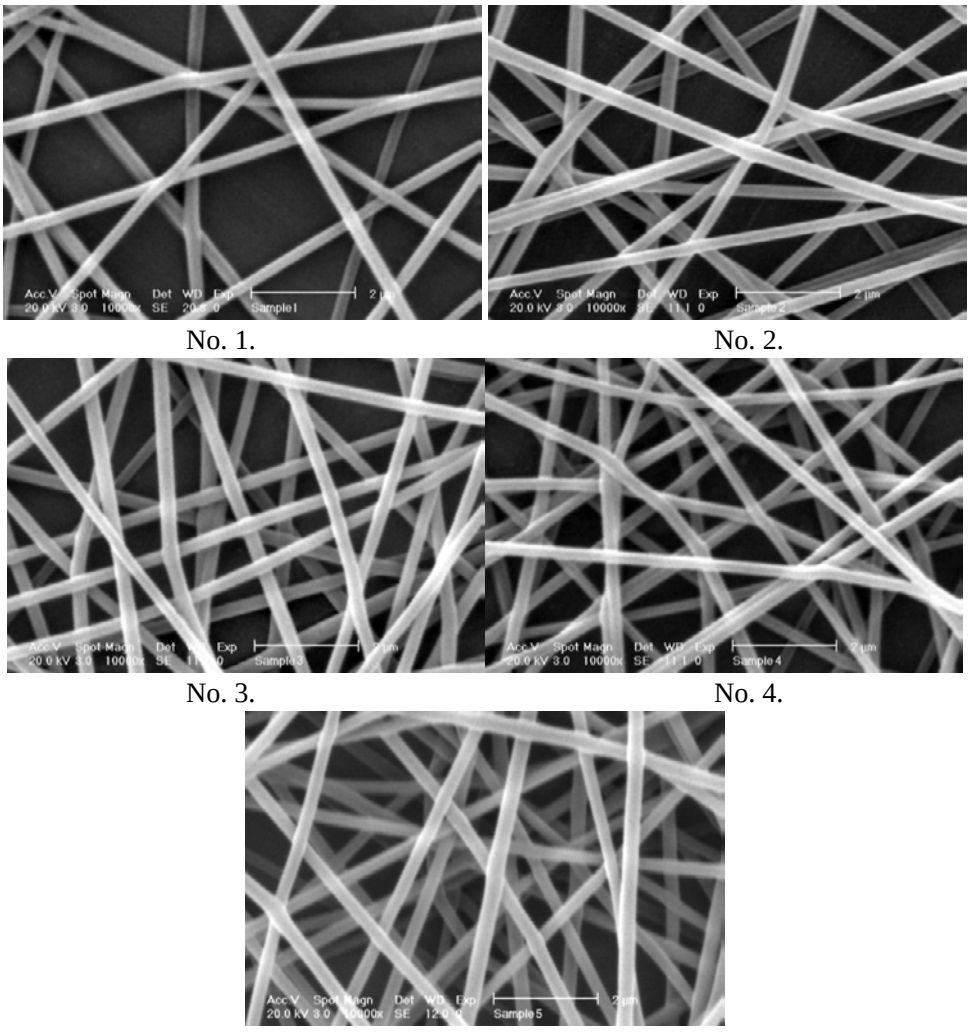

No. 1. No. 2.

No. 3. No. 4.

No.5.

Figure 5. Micrographs of the electrospun webs.

4. RESULTS AND DISCUSSION

Due to previously mentioned reasons, sieving methods and mercury porosimetry are not applicable for measuring pore structure parameters in nano-scale. The only method which seems to be practical is flow porosimetry. However, since in this study, the nanofibers were made of PVA, finding an appropriate liquid for the test to be performed is almost impossible because of solubility of PVA in both organic and inorganic liquids.

As an alternative, image analysis was employed to measure pore structure parameters in electrospun nanofiber webs. PSD curves of the webs, determined using the image analysis method, are shown in Figure 6. Pore characteristics of the webs (O_{50}, O_{95}, C_u, number of pores, porosity) measured by this method are presented in Table 2. It is seen that decreasing the porosity, O_{50} and O_{95} decrease. C_u also decreases with respect to porosity, that's to say

increasing the uniformity of the pores. Number of pores has an increasing trend with decreasing the porosity.

The image analysis method presents valuable and comprehensive information regarding to pore structure parameters in nanofiber webs. This information may be exploited in preparing the webs with needed pore characteristics to use in filtration, biomedical applications, nanoparticle deposition and other purposes. The advantages of the method are listed below:

1. The method is capable of measuring pore structure parameters in any nanofiber webs with any pore features and it is applicable even when other methods may not be employed.
2. It is so fast. It takes less than a second for an image to be analyzed (with a 3 GHz processor).
3. The method is direct and so simple. Pore characteristics are measured from the area of the pores which is defined as the number of pixels of the pores.
4. There is no systematic error in measurement (such as assuming pores to be cylindrical in mercury and flow porosimetry and the errors associated with the sieving methods which were mentioned). Once the segmentation is successful, the pore sizes will be measured accurately. The quality of images affects the segmentation procedure. High-quality images reduce the possibility of poor segmentation and enhance the accuracy of the results.
5. It gives a complete PSD curve.
6. There is no cost involved in the method and minimal technical equipments are needed (SEM for obtaining the micrographs of the samples and a computer for analysis).
7. It has the capability of being used as an on-line quality control technique for large scale production.
8. The results obtained by image analysis are reproducible.
9. It is not a destructive method. A very small amount of sample is required for measurement.

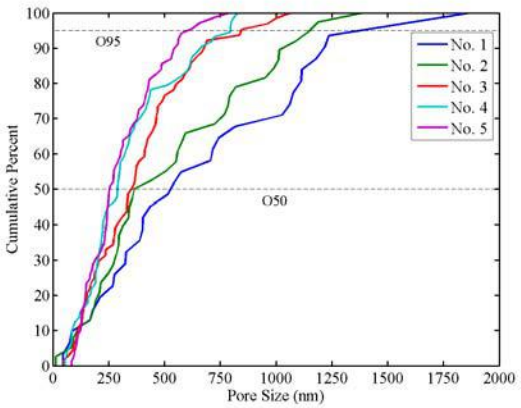

Figure 6. PSD curves of electrospun webs.

Table 2. Pore characteristics of electrospun webs

No.	O_{50}		O_{95}		C_u	Pore No.	Porosity
	pixel	nm	pixel	nm			
1	39.28	513.9	94.56	1237.1	8.43	31	48.64
2	27.87	364.7	87.66	1146.8	5.92	38	34.57
3	26.94	352.5	64.01	837.4	3.73	64	26.71
4	22.09	289.0	60.75	794.8	3.68	73	24.45
5	19.26	252.0	44.03	576.1	2.73	69	15.74

In an attempt to establish the effects of some structural properties on pore characteristics of electrospun nanofibers, two sets of simulated images with varying properties were generated. The simulated images reveal the degree to which fiber diameter and density affect the pore structure parameters. The first set contained images with the same density varying in fiber diameter and images with the same fiber diameter varying in density. Each image had a constant diameter. The second set contained images with the same density and mean fiber diameter while the standard deviation of fiber diameter varied. The details are given in Table 3 and Table 4. Typical images are shown in figure 7 and figure 8..

Table 3. Structural characteristics of first set images

No.	Angular Range	Line Density	Line Thickness
1	0-360	20	5
2	0-360	30	5
3	0-360	40	5
4	0-360	20	10
5	0-360	30	10
6	0-360	40	10
7	0-360	20	20
8	0-360	30	20
9	0-360	40	20

Table 4. Structural characteristics of second set images

No.	Angular Range	Line Density	Line Thickness	
			Mean	Std
1	0-360	30	15	0
2	0-360	30	15	4
3	0-360	30	15	8
4	0-360	30	15	10

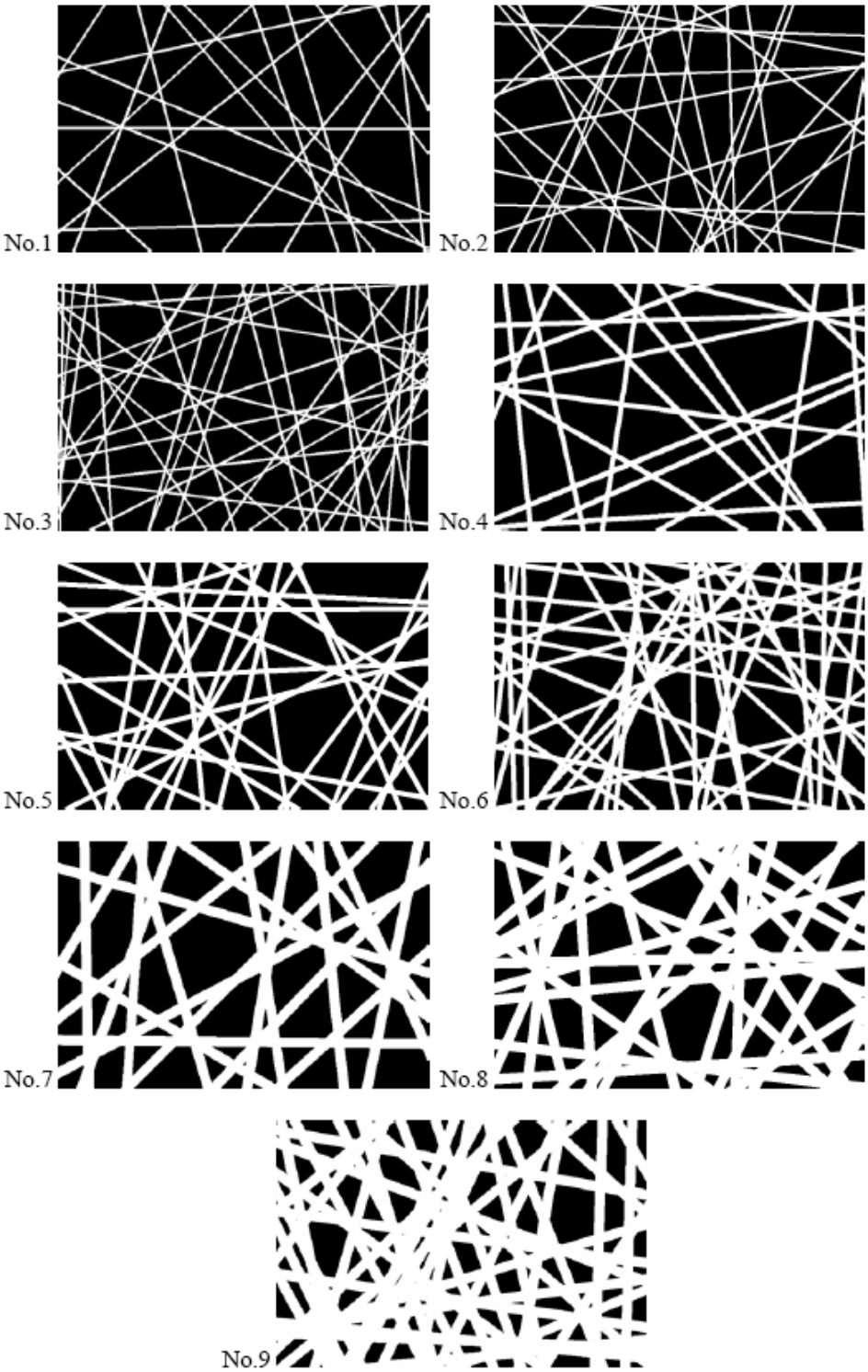

Figure 7. Simulated images of the first set.

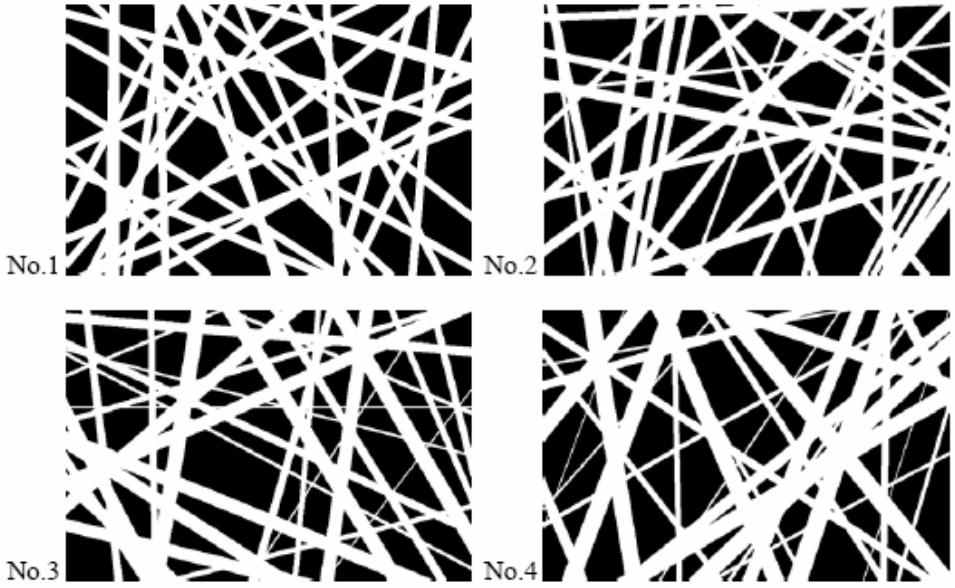

Figure 8. Simulated images of the second set.

Pore structure parameters of the simulated webs were measured using image analysis method. Table 5 summarizes the pore characteristics of the simulated images in the first set. For the webs with the same density, increasing fiber diameter resulted in a decrease in O_{95}, number of pores and porosity. No particular trends were observed for O_{50} and C_u. Figure 9 and figure 10 show the PSD curves of the simulated images in the first set. As the web density increases, the effects of fiber diameter are less pronounced since the PSD curves of the webs become closer to each other. For the webs with the same fiber diameter, increasing the density resulted in a decrease in O_{50}, O_{95}, C_u and porosity whereas number of pores increased with the density.

Table 5. Pore characteristics of the first set of simulated images

No.	O_{50}	O_{95}	C_u	Pore No.	Porosity
1	27.18	100.13	38.38	84	79.91
2	15.52	67.31	22.20	182	71.78
3	13.78	52.32	18.71	308	69.89
4	36.65	94.31	43.71	67	66.10
5	17.89	61.64	22.67	144	53.67
6	12.41	51.60	16.70	245	47.87
7	24.49	86.90	33.11	58	41.05
8	16.31	56.07	21.66	108	32.53
9	13.11	45.38	17.75	126	22.01

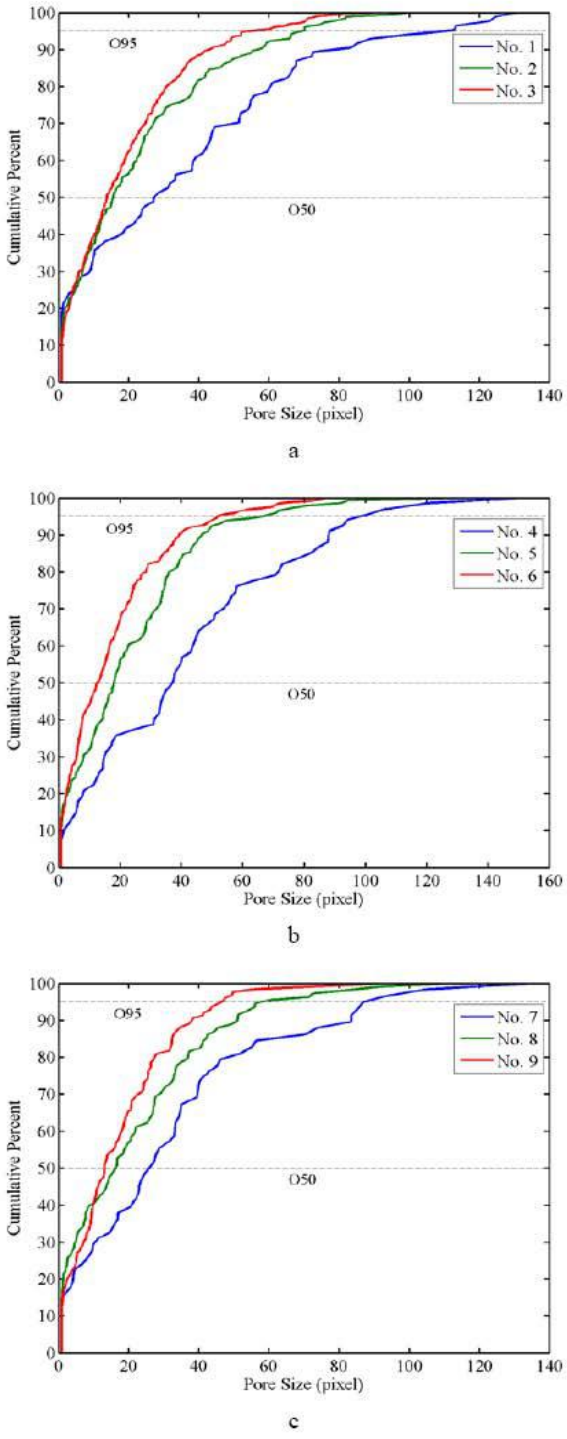

Figure 9. PSD curves of the first set of simulated images; effect of density, images with the diameter of a) 5, b) 10, c) 20 pixels.

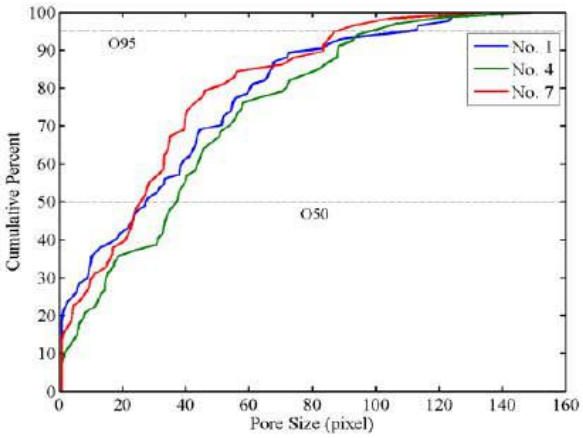

a

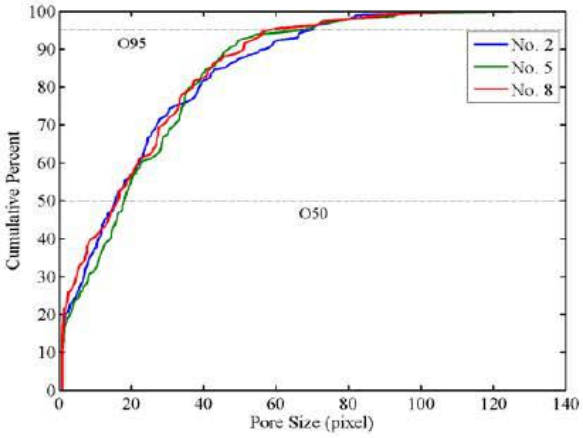

b

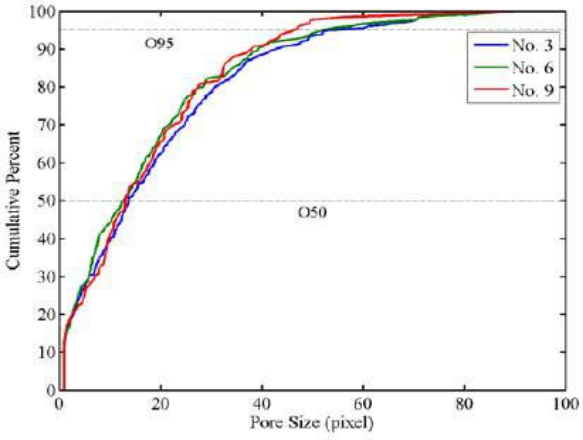

c

Figure10. PSD curves of the first set of simulated images; effect of fiber diameter, images with the density of a) 20, b) 30, c) 40 lines.

Table 6 summarizes the pore characteristics of the simulated images in the second set set. No significant effects for variation of fiber diameter on pore characteristics were observed. Suggesting that average fiber diameter is determining factor not variation of diameter. Figure 11 shows the PSD curves of the simulated images in the second set.

Table 6. Pore characteristics of the second set of simulated images

No.	O_{50}	O_{95}	C_u	Pore No.	Porosity
1	14.18	53.56	18.79	133	35.73
2	13.38	61.66	20.15	136	41.89
3	18.14	59.35	22.07	121	41.03
4	15.59	62.71	20.20	112	37.77

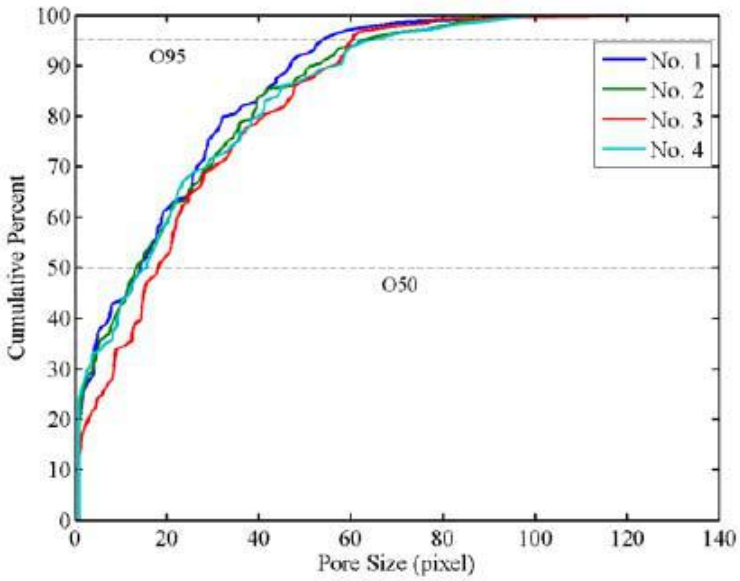

Figure 11. PSD curves of the second set of simulated images, the effect of fiber diameter variation.

5. CONCLUSION

The evaluation of electrospun nanofiber pore structure parameters is necessary as it facilitates the improvement of the design process and its eventual applications. Various techniques have been developed to assess pore characteristics in porous materials. However, most of these methods are indirect, have inherent problems and are not applicable for measuring pore structure parameters of electrospun webs. In this investigation, we have successfully developed an image analysis based method as a response to this need. The method is simple, comprehensive and so fast and directly measures the pore structure parameters.

The effects of web density, fiber diameter and its variation on pore characteristics of the webs were also explored using some simulated images. As fiber diameter increased, O_{95},

number of pores and porosity decreased. No particular trends were observed for O_{50} and C_u. Increasing the density resulted in a decrease in O_{50}, O_{95}, C_u and porosity whereas number of pores increased with the density. The effects of variation of fiber diameter on pore characteristics were insignificant.

REFERENCES

[1] A. K. Haghi, M. Akbari, Trends in Electrospinning of Natural Nanofibers, *Physica Status Solidi (a),* 204, 1830-1834 (2007).

[2] D. H. Reneker, I. Chun, Nanometre Diameter Fibers of Polymer, Produced by Electrospinning, *Nonotechnology,* 7, 216-223 (1996).

[3] D. R. Salem, Structure Formation in polymeric Fibers, Hanser, Cincinnati , Chapter 6, H. Fong, , D. H. Reneker, *Electrospinning and the Formation of Nanofibers.* (2001).

[4] Th. Subbiah, G. S. Bhat, R. W. Tock, S. Parameswaran, S. S. Ramkumar, Electrospinning of Nanofibers, *Journal of Applied Polymer Science,* 96, 557-569 (2005).

[5] A. Frenot, I. S. Chronakis, Polymer Nanofibers Assembled by Electrsopinning, *Current Opinion in Colloid and Interface Science,* 8, 64-75 (2003).

[6] Ch. L. Casper, J. S. Stephens, N. G. Tassi, D. B. Chase, J. F. Rabolt, Controlling Surface Morphology of Electrospun Polystyrene Fibers: Effect of Humidity and Molecular Weight in the Electrospinning Process, *Macromolecules,* 37, 573-578 (2004).

[7] W. Dierickx, Opening Size Determination of Technical Textiles Used in Agricultural Applications, *Geotextiles and Geomembranes,* 17 (4), 231–245 (1999).

[8] S. K. Bhatia, J. L. Smith, Geotextile Characterization and Pore Size Distribution: Part II. *A Review of Test Methods and Results, Geosynthetics International,* 3 (2), 155–180 (1996).

[9] S. K. Bhatia, J. L. Smith, B. R. Christopher, Geotextile Characterization and Pore Size Distribution: Part III. Comparison of Methods and Application to Design, Geosynthetics International, 3 (3), 301–328 (1996).

[10] S. T. Ho, D. W. Hutmacher, A Comparison of Micro CT with Other Techniques Used in the Characterization of Scaffolds, *Biomaterials,* 27, 1362-1376 (2006).

[11] A. H. Aydilek, T. B. Edil, Evaluation of Woven Geotextile Pore Structure Parameters Using Image Analysis, *Geotechnical Testing Journal,* 27 (1), 1-12 (2004).

[12] A. H. Aydilek, S. H. Oguz, T. B. Edil, Digital Image Analysis to Determine Pore Opening Size Distribution of Nonwoven Geotextiles, *Journal of Computing in Civil engineering,* 280-290 (2002).

[13] R. C. Gonzalez, R. E. Woods, Digital Image Processing, Prentice Hall, New Jersey, Second Edition (2001).

[14] B. Jähne, Digital Image Processing, Springer, England, 5th Revised and Extended Edition (2002).

[15] H. S. Kim, B. Pourdeyhimi, A Note on the Effect of Fiber Diameter, Fiber Crimp and Fiber Orientation on Pore Size in Thin Webs, *International Nonwoven Journal,* 15-19 (Winter 2000).

[16] M. S. Abdel-Ghani, G. A. Davis, Simulation of Nonwoven Fiber Mats and the Application to Coalescers, *Chemical Engineering Science,* 117 (1985).

[17] B. Pourdeyhimi, R. Ramanathan, R. Dent, Measuring Fiber Orientation in Nonwovens, *Part I: Simulation, Textile Research Journal,* 66 (11), 713-722 (1996).

In: Monomers, Oligomers, Polymers, Composites… ISBN: 978-1-60456-877-6
Editors: R. A. Pethrick, G.E. Zaikov et al.

Chapter 12

INTERPOLYMERIC ASSOCIATIONS BETWEEN ALGINIC ACID AND POLY (N-ISOPROPYLACRYLAMIDE), POLY (ETHYLENE GLYCOL) AND POLYACRYLAMIDE

Catalina Natalia Duncianu and Cornelia Vasile
„Petru Poni" Institute of Macromolecular Chemistry,
41 A, Gr.Ghica Voda Alley, 700487, Iasi, Romania

INTRODUCTION

It is well-known that hydrogen bonding and polyelectrolyte complexes are two categories of intermacromolecular (interpolymeric) associations depending on the type of the interacting forces between polymeric constituents. H-bonding complexes result by the interaction between a proton donating polymer (weak polyacid) and a proton accepting polymer (a weak Lewis polybase) via hydrogen bonds. They can be formed between the protons low density region and a high electron density charge region. The proton acceptor polymers can interact with proton donor polymers in aqueous solution or organic solvents [1, 2]. The interest for these interpolymeric complexes (IPC) can be explained because of their unique physical and chemical properties in comparison with pure components. The hydrogen-bonded IPCs have attracted a great attention of pharmaceutical scientists due to the wide possibilities of their use in the development of different drug formulations [3, 4, 5, 6, 7, 8]

It is well-known that IPC formation and stabilization are due to the cooperative hydrophilic and hydrophobic effects and depend on: the composition of the system, structure of the polymers, concentration of polymer solution, pH, temperature, ionic strength, etc. [1, 3, 9, 10].

Several authors reported IPC's formation between the proton donating polymer (e.g. poly(acrylic acid)- PAA, poly(methacrylic acid)-PMMA), and the proton accepting polymer (e.g. poly (ethylene glycol)- PEG, poly (acrylamide)- PAM, poly(N-isopropylacrylamide)-PNIPAM) in aqueous solutions. [11, 12, 13, 14] or polyacid copolymers with different polybases [15, 16]. Only few studies deal with the IPC formation using a polysaccharide as a

weak polybase [17, 18, 19, 20]. They found that by using a polycarboxylic acid as a proton donor polymer, the complex formation will depend on pH of the solution and, of course, on the dissociation degree of the polyacid. The dissociation of the acid is crossed out in the presence of the Lewis base (e.g. PEO) and can be estimated via an apparent dissociation constant (Kd). The existence of an amount of undissociated carboxylic groups (COOH) is a condition for obtaining a stable complex through hydrogen bonds. Thus, this condition is accomplished at a certain pH when the complex can be irreversibly formed. During the last decade, the researchers interest have been caught by the intermacromolecular associations between non-complementary polymers containing variable number of functional groups on the mole unit like polysaccharides, random, alternant [21] or graft-copolymers as they can be better simulate the intermolecular interactions between natural complex macromolecules. In addition to H-bonding, hydrophobic interactions contribute to the formation and stabilization of the IPCs [22]

Using a natural polymer as weak polyacid e.g. alginic acid to obtain interpolymeric complexes mainly with chitosan represents an attractive target for many researchers especially due to its applications in the drug delivery systems [23, 24] and pharmaceutics [25]

In the present work, it has been studied the interpolymeric associations between alginic acid (AgA) with poly (N-isopropylacrylamide) (PNIPAM), poly (ethylene glycol) (PEG) or poly (acrylamide) (PAM) by using the following methods: viscosity, pH-metry and conductivity measurements.

2. EXPERIMENTAL

2.1. Materials

Alginic acid is a natural hydrophilic polysaccharide which is extracted from different brown seaweeds (*Macrocystis pyrifera, Ascophyllum nodosum*).

Alginic acid can be found in three different structures depending on the type of the seaweed extracted from. One of it's structure can have only blocks of L- Guluronic acid (G), a second one can contain only segments of D- Manuronic acid (M) and the last one can have an alternated structure between D- Manuronic and L- Guluronic units (scheme 1).

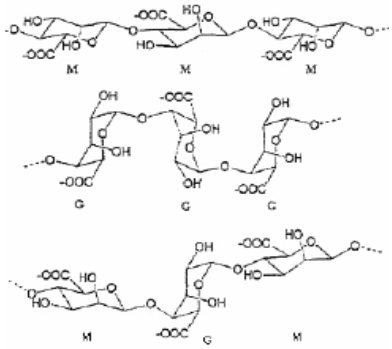

Scheme 1. Structural formulas of alginic acid (AgA) [26, 27].

The commercial alginic acid used in this study is a Fluka product with an average molecular weight of 48,000-186,000 [9005-32-7] (according to Fluka specifications), the reduced viscosity in water at 25 ^{o}C for an aqueous solution of c= 0.2 wt % is η_{red} =2.41 ml*g^{-1}, a drying loss ≤ 10 wt % and ash ≤ 3%.

Poly (N-Isopropylacrylamide), PNIPAM

The polymers with a low critical solubility temperature (LCST) presents a great interest in green chemistry field, catalysts, drug delivery, sensors, permeability control in composites used as films. PNIPAM is the most representative of this class of polymers because it shows a phase transition at a low critical solubility temperature at about 31- 33 ^{o}C, close to physiological temperature [34]. Aqueous solutions based on PNIPAM, are the best examples of thermo-sensitive materials. It can be observed that it precipitates above LCST and it re-dissolves below it. It has been shown that, in the case of PNIPAM, the behavior is due to hydrophobic N-alkyl groups (see scheme 3) and solvent type.

LCST is the result of the variation of entropy at the dewatering of the amidic groups with the increase of the temperature and it can be influenced by the content of salts, alcohols, surfactants addition. In this way, pH of solution is varying also. LCST varies in a range close to human body temperature; so, the PNIPAM was proposed to be used in biological applications.

With the increase of the temperature, PNIPAM configuration suffers some changes regarding the shape of the chain leading to reversible swelling-deswelling properties. [35] These properties can be useful in the control process of the thickness of the gels layers and their composition. PNIPAM gels can show temperature sensitive phase changes and they can be used as sensors or actuators.

In this study PNIPAM was synthesized via free radical polymerization of N-isopropylacrylamide in water at 30 ^{o}C using the redox system of ammonium persulfate $(NH_4)_2$ S_2O_8, with potassium bisulfite, $K_2S_2O_5$. [36] The resulting product was purified by dialyse against water through a membrane (cut off ~12 000 Dalton, Sigma) and freeze drying. The average viscometric molecular weight of PNIPAM, measured at 20ºC in 0.5 M $LiNO_3$ aqueous solution is 28 000 Dalton.

Poly (ethylene glycol) (PEG) is a linear, water-soluble polymer and it can be obtained by an addition reaction of ethylene oxide (or ethylene glycol). Its general formulae is:

$$H\text{-}(OCH_2CH_2)_n\text{-}OH$$

where “n" is the polymerization degree.

PEG is widely used in pharmaceutical industry and cosmetics; it is non-volatile and inert from physiologically point of view. It posses moderate swelling properties. According to its molecular weight it can show different viscosity values and different properties [28]. For example, PEG with a molecular weight of about 2000 can be used as thickening agent for shaving creams emulsions, teeth paste, different creams and hair conditioner production. The compound with a high molecular weight can be used as suspension and thickening agent for washing powders, soaps, cosmetics.

In pharmaceutics, PEG can be used for the different ointments, emulsions, pastes, lotions and suppositories production. [29]

In this study, a PEG with a molecular weight 35,000 and with a melting temperature of 60-65^{0}C was used.

Poly (Acrylamide) (PAM)

In last decades poly (acrylamide) (PAM) had been identified as an efficient polymer both from ecological point of view mainly for infiltrations and erosions preventing in agriculture. [30, 31] It has the following formulae (scheme2):

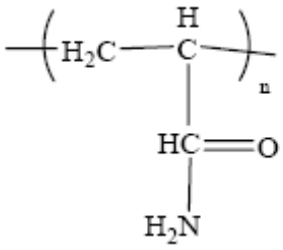

Scheme 2. Poly (acrylamide) structure.

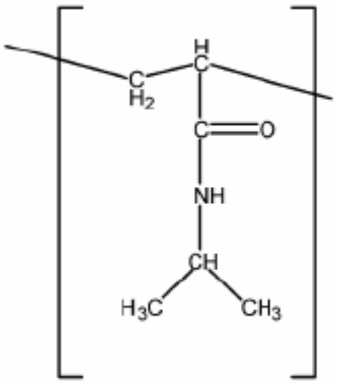

Scheme 3. Poly (N-isopropylacrylamide) (PNIPAM) structure.

PAM can be successfully used in efficient technologies for soil treatment and to improve the infrastructure (roads). [32]

PAM with high molecular weight is used as conditioning agent being added in the water used for irrigations.

PAM is used as flocculant agent in minerals processing and industrial wastes treatment. Copolymers based on acrylamide enhance the paper resistance.

The PAM used in our study was synthesized in a 5% water solution of acrylamide (Sigma) using hydrogen peroxide as initiator at 50 ^{o}C. [33] It was then precipitated in methanol, dissolved in water and freeze dried. Its molecular weight was viscometrically determined and it was found to be 1.5 * 10^5 Dalton.

2.2. Preparation of the Aqueous Solution of PEG, PAM, PNIPAM, Aga in Twice Distilled Water

To minimize the polymer – polymer interactions effect, the diluted aqueous polymers solutions were prepared, all with the same concentration of 0.2 wt %. Twice distilled water was used for the preparation of the solutions. The pH of each solution was measured and they were of 3.21; 5.3; 5.4 and 5.5 for AgA, PNIPAM, PEG and PAM, respectively.

The pH of each polymer solution was adjusted at pH ≈ 4 by adding several drops of 2 M NaOH or HCl, corresponding with the minimum value for alginic acid to be dissolved.

Alginic acid solution adjusted at pH = 4 was filtered to remove undissolved particles. The real concentration of the polymer solution had been determined after filtration by evaporation of a certain volume of solution and weighing the dry mass. The alginic acid solutions was mixed with each polybase solution (PNIPAM, PEG or PAM to obtain binary mixtures in various ratios; so the entire range of composition of AgA/ polybase (PNIPAM, PEG or PAM) mixtures was covered from 5 wt % to 95 wt % AgA.

2.3. Investigation Methods

Viscometry

Viscometric experiments have been performed by means of an Ubbelhode type viscometer with dilution and suspended level, at 25 °C ± 0.02 ° C and flow times were measured with an accuracy of ± 0.1s. The reduced viscosity (ηsp /c) was determined for each partner solution and their binary blends in different weight ratios. The ideal value of the viscosity of the mixture solution can be calculated by using the equation (1) assuming the simple additivity of the viscosities of the solutions of components if there are no interactions between them. Equation (1) is applicable only for non-ionic (non polar) components.

$$\eta_{red,\,id} = \eta_1 * \omega_1 + \eta_2 * \omega_2, \quad (1)$$

η_1, η_2 are the reduced viscosities of the pure components from the system; ω_1, ω_2 are the weight fractions of the polyacid and polybases, respectively.

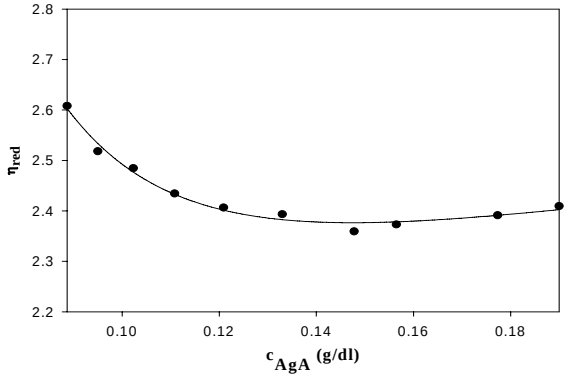

Figure 1. Dilution curve of alginic acid in twice distilled water.

In the study conditions, as it appears from dilution curve of AgA, in figure 1, the alginic acid behaves like a weak polyelectrolyte. Thus, the reduced viscosity records an increase with the decreasing of concentration of the polyacid.

In this case it is necessary to apply another equation for the evaluation of the ideal reduced viscosity of the system [11, 12, 37], namely:

$$(\eta_{sp} / c)_{calc} = w_1 * (\eta_{sp\ 1} / c1) + w_2 * (\eta_{sp\ 2} / c), \quad (2)$$

$\eta_{sp\ 1} / c_1$ is the reduced viscosity of the polyacid at the concentration c_1; η_{red1} as (η_{sp1} / c_1) can be determined from the dilution curve of AgA (figure 1) being dependent on the real concentration of AgA within the system (c_1).

η_{sp2}/c is the reduced viscosity of the polybase at the total polymer concentration in system, c; w_1, w_2 are the weight ratios of the two polymers in the solution mixture.

To distinguish better the interactions in all three studied systems, it had been introduced the ratio between the experimental value and the calculated one, named viscosity ratio (equation 3) [38, 39]:

$$r_\eta = \eta_{exp} / \eta_{calc} \quad (3)$$

η_{exp} is experimental value of the reduced viscosity of the polymer mixture ; η_{calc} is the calculated value of the reduced viscosity of the polymer mixture by using equation (2).

When r_η takes values lower than unity it means that the formed interpolymeric complex via hydrogen bonds has a rather compact structure in comparison with that of the pure components. In this case the system shows a contraction of the polymers conformation due to the presence of the hydrogen bonds. [11, 12, 14, 18, 40]

A value higher than unity indicates an expansion of the complex conformation which leads to the appearance of a gel like structure. [12]

An ideal behavior is marked by a value equal with the unity. In this case the two polymers, practically, do not interact at all.

pH Measurements

pH measurements were performed at 25 °C ± 0.02 ° C, in a thermostated bath, with a Consort C835 multimeter equipped with a separate pH glass electrode suitable for diluted solutions domain.

Conductometry

The conductivity measurements were carried out by using a Consort C 835 multimeter equipped with a separate conductivity glass electrode specific to the measurements in 0.1µS-1000 mS range, characteristic for diluted polymer solutions.

To evidence better the formation of hydrogen bonds between the polymers in aqueous solutions, the “iso-pH” method was applied which consists in measurements of all characteristics starting with solutions of components having the same values of pH. [11, 12, 13, 14, 41, 42]. In such conditions, the binary solutions obtained by mixing of the weak polyacid with weak polybase solution will present or not deviations of experimental values in respect with additive ones only because of some intermacromolecular interactions between polymers.

3. RESULTS AND DISCUSSIONS

3.1. Viscosimetry

Studying the system AgA/ PNIPAM, it had been found the values of the viscosity ratio (r_η) lay below 1 (figure 1). This means that within this system some interpolymeric associations are formed, having a compact structure with a maximum of deviation at weight of 15- 70% AgA / 85- 30% PNIPAM.

For the systems AgA/ PEG and AgA/ PAM have been found different behaviors depending on the composition range. In the range 2- 38% AgA/ 98-62% PEG or 18-52 % AgA / 82-48% PAM there are positive values of the viscosity ratio. The maximum value of the ratio it was found at weight of 2-20 % AgA/ 98-80% PEG and 18-40 % AgA/ 82-60% PAM, respectively- figure 1. In the second region (62-100% AgA/ 38-2% PEG or PAM- figure 1) it can be noticed that the value of the viscosity ratio is tending to unity; it means that, in this composition range the polymers do not interacting each other anymore.

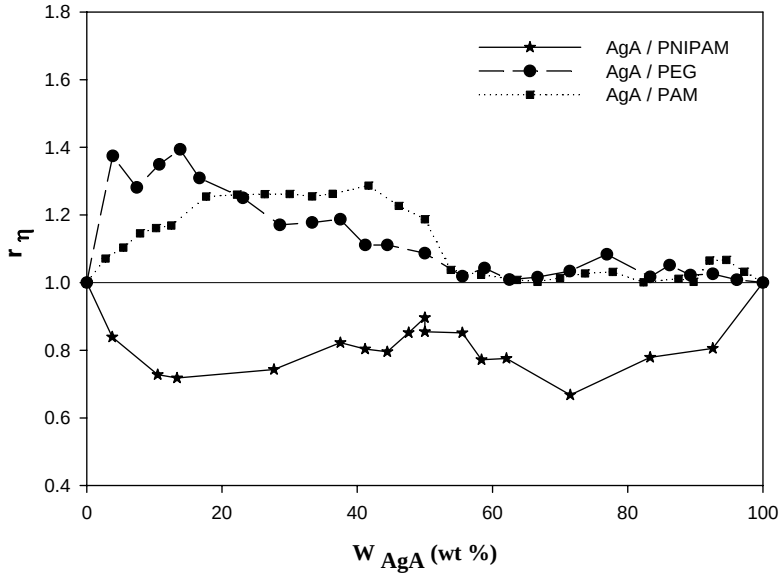

Figure 2. The dependence of the viscosity ratio on the composition of the systems: AgA/ PNIPAM (∗), AgA/ PEG (•), AgA/ PAM(■) in twice-distilled water at 25 ^{o}C.

3.2. pH – Measurements

The pH-measurements represent a useful method for the identification of the presence of an interpolymeric complex in protic solvents. The complexation process due to the hydrogen bonds formed between COOH groups of the polyacid and basic groups (-OH, -O-, -NH_2) of the polybase can change the pH of the solution.

Addition of the polybase to polyacid is leading to the increase of the pH of the solution till a constant value when the complexation equilibrium is established. Therefore, the –COOH groups concentration will decrease and, according to the dissociation equilibrium of the

polyacid, the concentration of the dissociated groups will decrease also at higher values of pH. [1, 14, 42]

Interpolymeric complexation between a polyacid (PA) like alginic acid (AgA) and a polybase (PB) like poly (N-isopropyl acrylamide) (PNIPAM) , poly(ethylene glycol) (PEG) or poly(acrylamide) (PAM) takes place according to a complexation equilibrium as following:

$$PA + PB \leftrightarrow C,$$

Equilibrium reaction is characterized by the apparent complexation constant:

$$Kc = [C] / [PA] [PB] \quad (4)$$

where: [C] is complex concentration; [PA], [PB] are the uncomplexed polyacid and polybase concentrations.

The complexation process takes place via the successive hydrogen bonds between the reactive groups:

$$-COOH + B \leftrightarrow -COOH...B$$

The acidic groups are dissociated according to dissociation equilibrium

$-COOH \leftrightarrow COO^- + H^+$ characterized by dissociation constant Kd:

$$Kd = [COO^-]^* [H^+]/ [COOH], \quad (5)$$

The association degree can be determined according to the equation (6). [13]

$$\theta = 1- ([H^+]/ [H^+]_0)^2 \quad (6)$$

where:

- $[H^+]$, $[H^+]_0$ are the hydrogen concentrations in the presence and absence of the acceptor polymer
- θ – association/dissociation degree of the –COOH groups of the polyacid.

$$pKd= a+ b^* pH \quad (7)$$

Dissociation constant, K_d has been obtained by using Kern empiric equation (eq 7) [43] and some blank experiments which consist in measurements of the pH of the pure alginic acid at different concentrations and different temperatures in the absence of the polybase solutions and the linear dependences as in figure 3 were obtained for all temperatures tested.

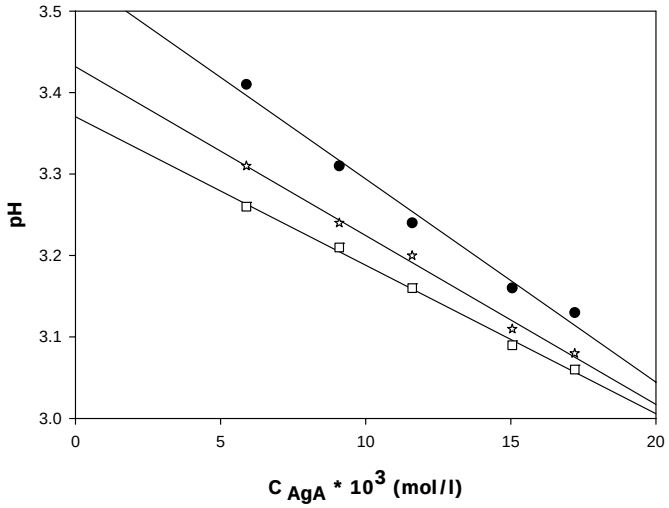

Figure 3. The dependence of the pH on the alginic acid concentration, C_{AgA}, at 25 °C (•), 30 °C (∗) and 35 °C(■).

From the linear dependence of the calculated pKd according equation (7) pKd values of alginic acid at different pH values are shown in figure 4.

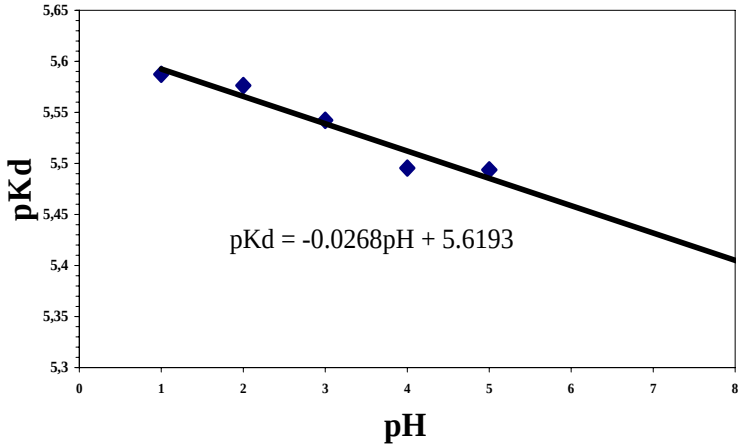

Figure 4. pKd - pH dependence for the alginic acid solution in twice- distilled water.

The behaviour of a polyelectrolyte can be decribed also by the Henderson-Hasselbalch equation according to the disociation equilibrium of the polyacid and eq. (5):

$$pKd = pH + \log_{10} [COO^-]/[COOH] \quad (8)$$

Kagawa and Tsumura [44- ref 3 therein], in their study on the carboxymethylcellulose dissociation found that Kern formula [43] has a good applicability in the individual experiments series under fixed conditions like dilution or neutralization studies but it lacks universal applicability. Kagawa transformed Kern's equation according to his opinion that the

dissociability of polyelectrolytes should be dependent on the degree of dissociation [44- ref 6 therein].

Nagasawa and Rice [45] showed the equivalence between the two equations as being the equation of a titration curve obtained in the potentiometric titration of a polyacid with a polybase.

$$pKd = pH + n\log_{10}(1-\theta)/\theta \quad (9)$$

where n- empirical parameter,

θ dissociation degree, $\theta = [-COO^-] / [-COO^-] + [-COOH]$

Therefore in the present study we focused on the using of the Kern empirical equation (equation 7) to determine the dissociation constant of the alginic acid and thus the stability constants of the interpolymeric associations between alginic acid and PNIPAM, PEG and PAM. It was evaluated also the complexation degree (θ)-equation 6- and the thermodynamic characteristics-according to the equation 12.

Potentiometric curves from the figures 5 a, b, c show large maxima of pH which become even larger when temperature increases. These maxima are not very specific with type of system studied. They range between 16 – 70 wt% AgA for the system AgA/PNIPAM and 15 – 45 wt % in the case of AgA/PEG si AgA/PAM. This should mean that, if the intermacromolecular associations exist, they are not stoichiometrical. It is possible that temperature increase favors the solubility of the alginic acid the chain is extended increasing the number of intercontacts between components. This can be explained also by the fact that with higher temperature there are more accentuated interactions between components. [42] Another reason should be that in the working conditions we are at the limit between H-bonding or electrostatic interactions between components.

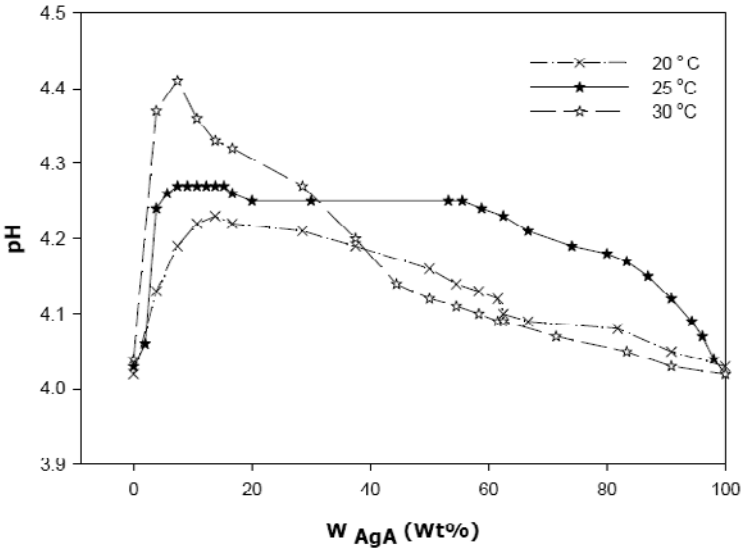

a

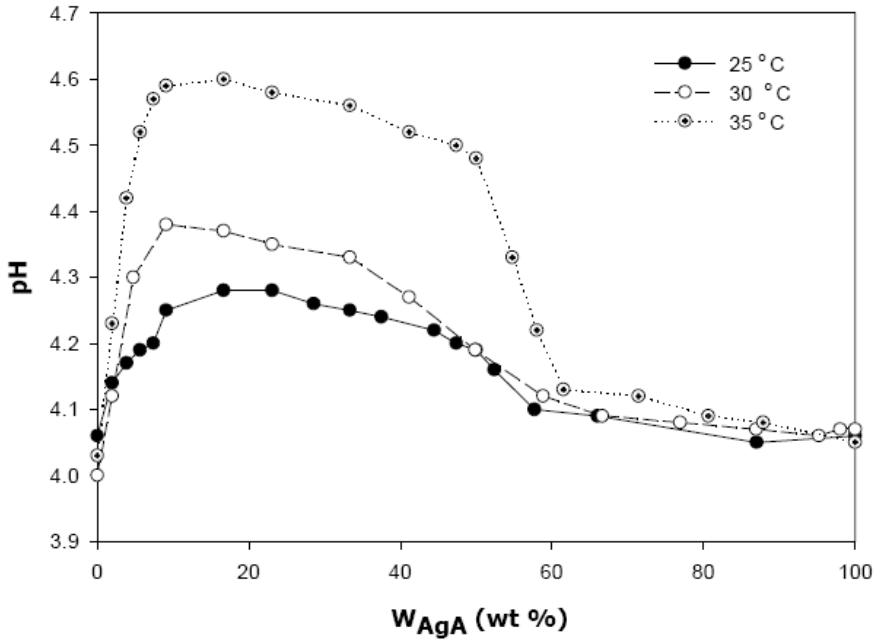

b

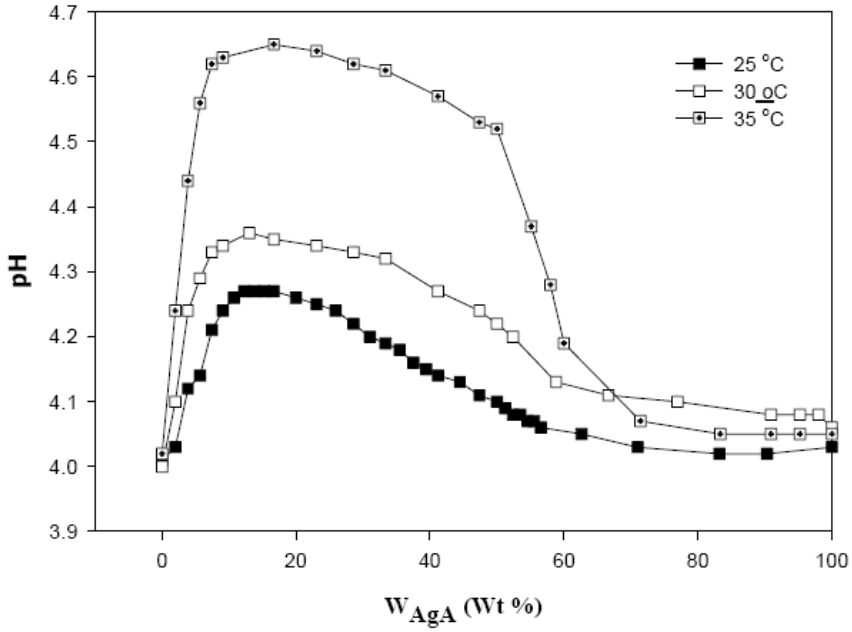

c

Figure 5. pH- values recorded at AgA titration with PNIPAM (a), with PEG (b) and PAM (c) at different temperatures.

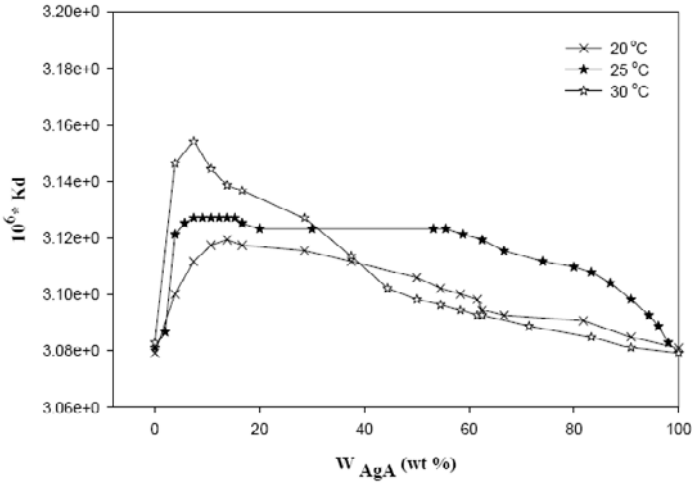

a

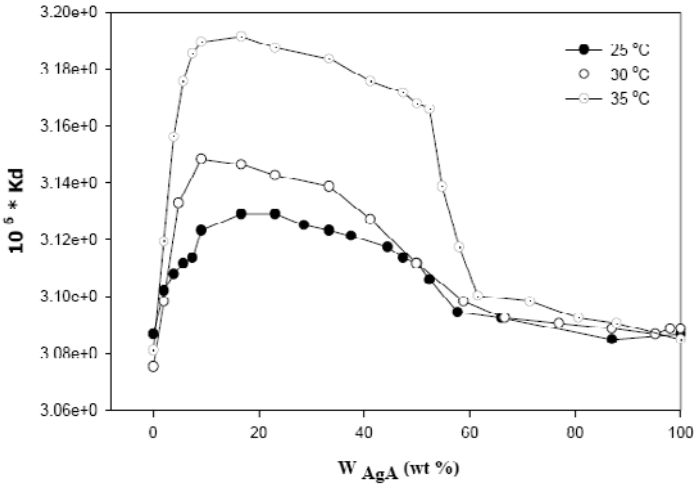

b

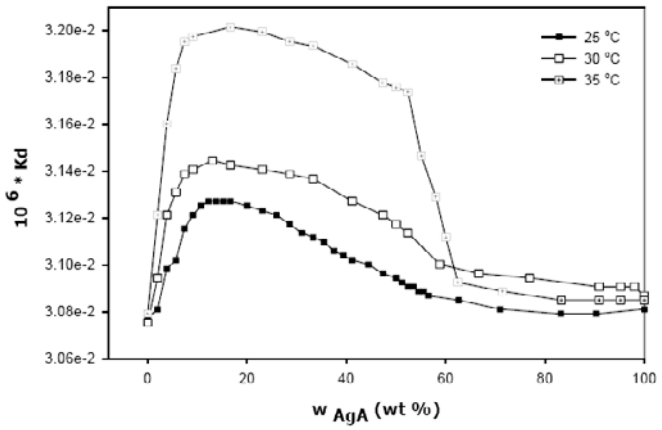

c

Figure 6. The dependence of the dissociation constant (Kd) on the system composition of AgA/ PNIPAM (a) AgA/ PEG (b) and AgA/ PAM (c) at different temperatures.

A similar dependence was found for variation of the the dissociation constant (Kd) with composition of the system – figure 6 and also of the interpolymeric associations concentration – figure 7.

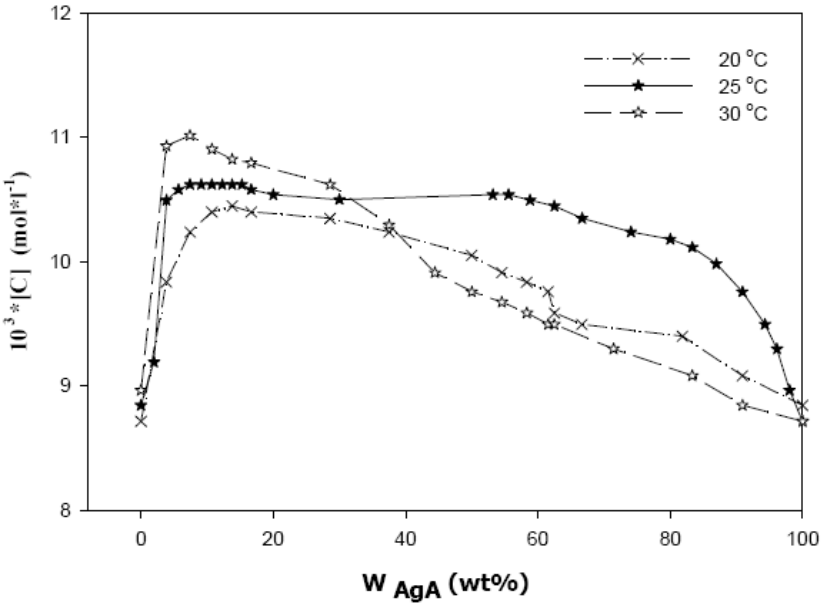

a

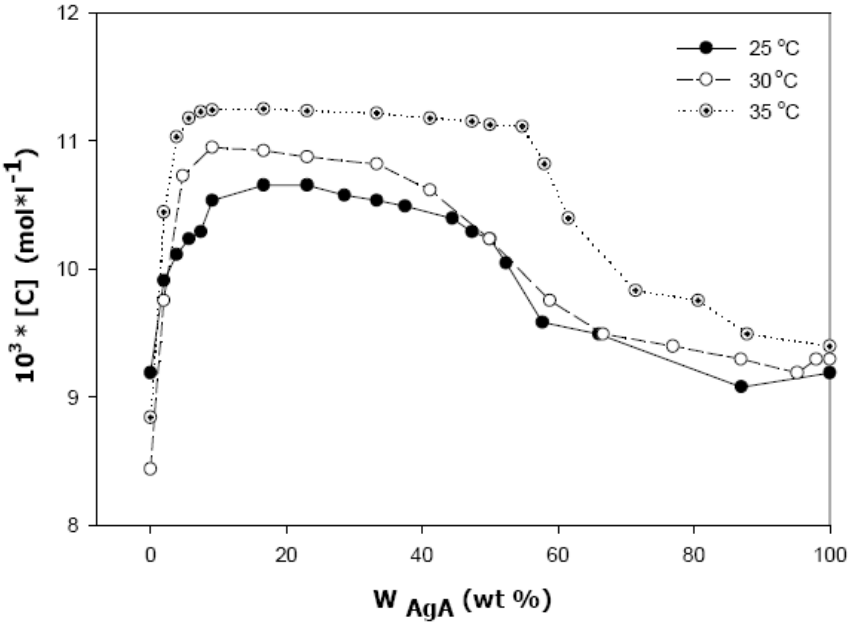

b

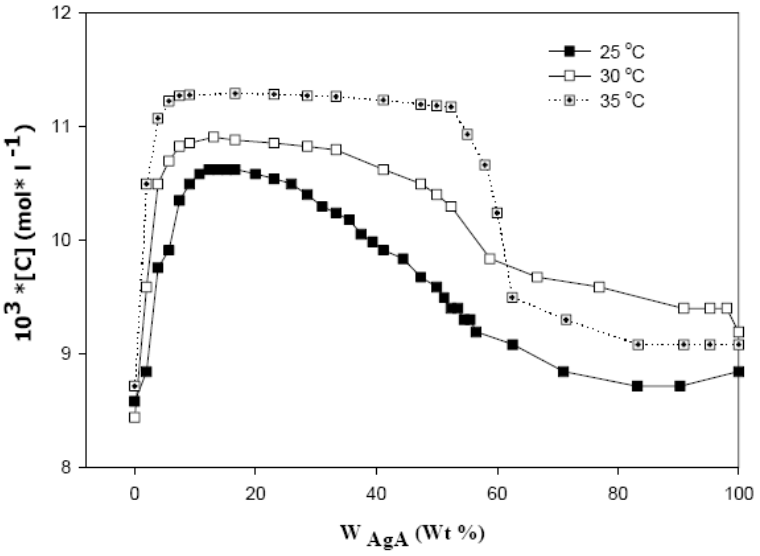

c

Figure 7. Variation of the complex concentration for the system AgA/ PNIPAM (a); AgA/ PEG (b) and AgA/ PAM (c) at different temperatures.

Interpolymeric complex concentration can be obtained by applying the mass conserving law for –COOH groups of the polyacid:

$$[C]= [AgA]_0- [COOH]- [COO^-], \quad (10)$$

Where:

[COOH] – molar concentration of –COOH uncomplexed groups;

[COO^-]- concentration of –COO^- groups which are uncomplexable.

[COO^-] was obtained from the equation which expresses solution the electroneutrality (equation 11), taking into account that the AgA solution pH had been adjusted to pH≅ 4 by using a solution of NaOH 0.2 M, and according isoionic dilution. [14, 42]

$$[COO^-]= [H^+] - [HO^-] \quad (11)$$

Similar procedures had been used for the determination of stability constants of the formed complexes and thermodynamic parameters of the complexation process of other systems. [9, 13, 46]

The concentrations of the interpolymeric associations are very low being of $1.062 * 10^{-2}$ (mol* L^{-1}) for AgA/ PNIPAM; $1.065* 10^{-2}$ (mol* L^{-1}) for AgA/PEG and $1.06 * 10^{-2}$ (mol* L^{-1}) for AgA/PAM system.

Association degree, θ, as a function of the system composition is plotted in figure 8. Its values are of 0.66, 0.63 and 0.69 for AgA/PNIPAM, AgA/PEG and AgA/PAM systems.

The dependence of the θ on the composition has the same shape as other characteristics of the intermacromolecular associations presented above as: pH, Kd, complex concentration.

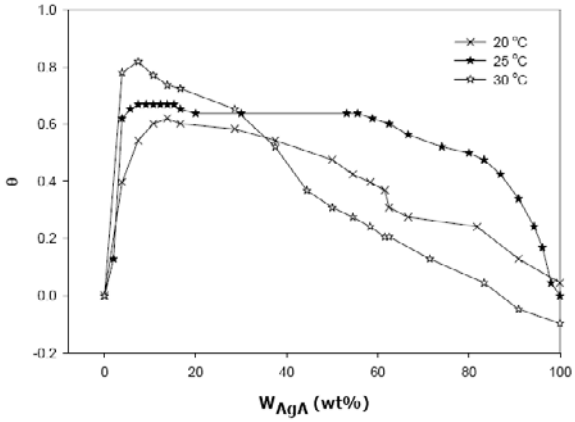

a

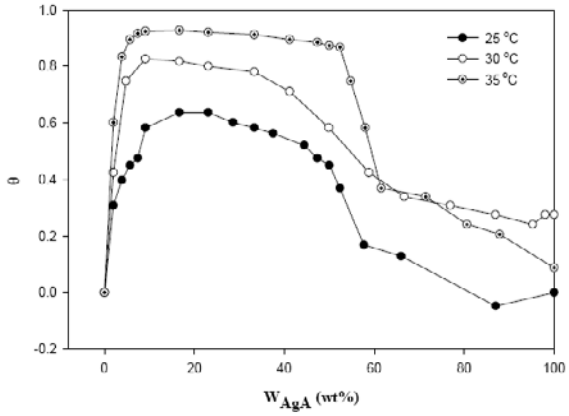

b

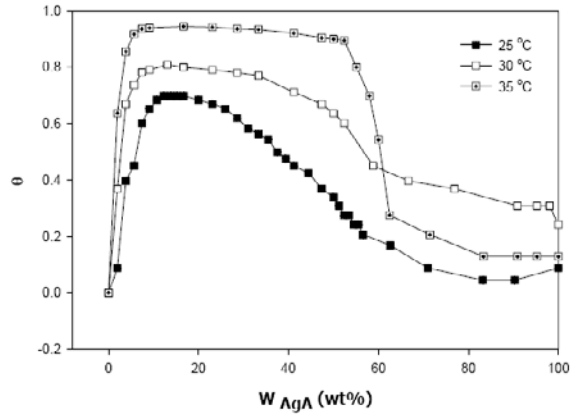

c

Figure 8. The dependence of the association degree on the system composition in the case of mixture AgA/PNIPAM (a); AgA/ PEG (b) AgA/ PAM (c) at different temperatures.

The average values of the equilibrium (stability) constants, Kc, calculated according equation 4, of the interpolymeric associations corresponding to the studied systems AgA/ PNIPAM, AgA/PEG, AgA/ PAM are given in the table 1 and figure 9.

Figure 9 displays the variation of the apparent complexation constant of AgA/ PNIPAM, AgA/ PEG, AgA/PAM with the weight fraction of alginic acid. It can be observed that the values of apparent complexation constant laid in close limits given above and are independent on polymer mixture composition.

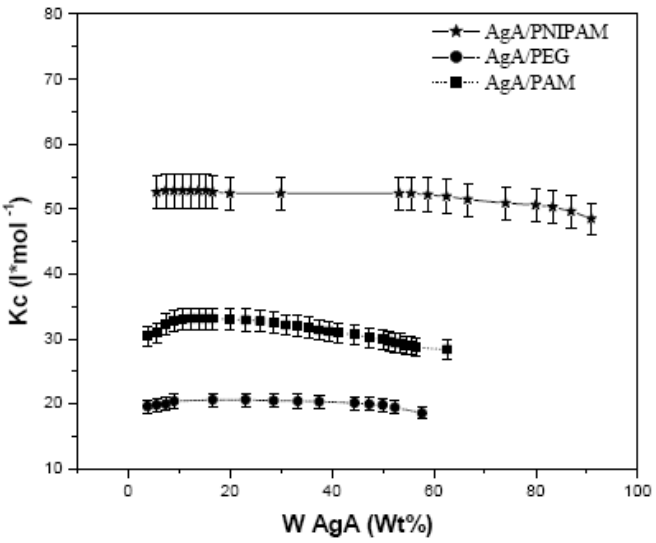

Figure 9. The dependence of the stability constant, Kc, of the system AgA/ PNIPAM, AgA/ PEG and AgA/ PAM on the composition (a).

Table 1. Values of the stability constants, Kc, for the studied systems at different temperatures

T (°C)	$Kc_{AgA/\ PNIPAM}$ ($L*mol^{-1}$)	$Kc_{AgA/\ PEG}$ ($L*mol^{-1}$)	$Kc_{AgA/\ PAM}$ ($L*mol^{-1}$)
20	51.94	-	-
25	52.80	20.64	33.14
30	54.76	21.20	34.02
35	-	21.78	35.22

The average values have been evaluated for the composition range where maxima in pH values and other characteristics were found for each system. At different temperatures there is a slight increase of Kc from 51.9 till 54.76 for AgA/PNIPAM system, from 20.64 till 21.78 for AgA/PEG system and from 33.1 till 35.2 for AgA/PAM system, this being an indication for the presence of the hydrophobic forces within the systems in the case of AgA/PNIPAM for which the Kc takes the highest values.

The van't Hoff dependence of ln Kc versus 1/T estimated according to eq. 12 and plotted in figure 10.

$$-\ln Kc = \Delta H - T\,\Delta S \quad (12)$$

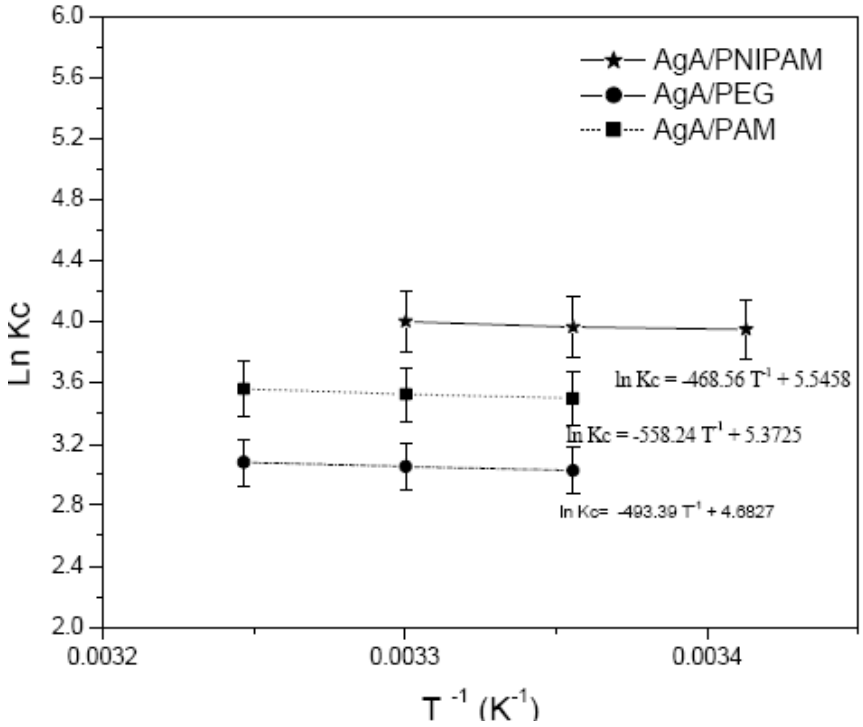

Figure 10. The dependence ln Kc= f (1/T) for the mixtures AgA/PNIPAM, AgA/PEG, AgA/PAM.

The values of the stability constants determined above and its variation with temperature show that the stability of the associations formed in the case of AgA/ PNIPAM, AgA/PEG and AgA/ PAM are not significantly influenced by the temperature variation.

It allows also the evaluation of the enthalpy and entropy of hydrogen-bonded associations from the slope and the intercept of the van't Hoff plot yielding for ΔH the values of - 3.89 KJ * mol^{-1} for AgA/ PNIPAM, -4.1 KJ*mol^{-1} for AgA/ PEG and - 4.6 KJ*mol^{-1} for AgA/PAM systems. (table 2).

Table 2. Estimated values for the enthalpy and entropy for the studied systems

System	ΔH (KJ*mol^{-1})	ΔS (J*mol^{-1}*K^{-1})
AgA/ PNIPAM	- 3.89	46
AgA/ PEG	- 4.1	38.9
AgA/ PAM	- 4.6	44.6

The obtained values of enthalpy are comparable with those evaluated by Tsushida [47] within the study of interpolymeric complexes based on poly (methacrylic acid), (PMMA) and poly (N-vinyl-2-pyrolidone), (PVPo) and poly (ethylene oxide). In comparison with the general hydrogen bond enthalpy (which is about 5 kcal/mol), the obtained experimental values are low and it can be attributed to the fact that only some of the active sites are

involved in the formation of the complexes and the employed conditions are at the limit of H-bond formation.

3.3. CONDUCTOMETRY

In the last years, conductometry had become an important analysis instrument of the counterions distribution in aqueous diluted polyelectrolytes solutions. The counterions influence the polyelectrolyte solution properties by their size, valence and polarizability. Conductometry measures the transport of all charged species within studied system. [48] Most of conductometric studies showed a slight increase of the conductivity with the decrease of concentration of polyion followed by an important increase of conductivity at high dilution. [49, 50, 51, 52, 53] Another studies reported that the conductivity can be independent on concentration [54] or it can show a minimum value especially in the case of cationic polyelectrolytes with quaternary ammonium salts groups. [55, 56] Studying the conductometric behavior of some cationic polysaccharides, Ghimici [57] had observed an almost linear increase of conductivity with the dilution over a wide concentration range. Wandrey had taken into account the influence of macromolecular parameters and the chemical structure on the polyion- counterion interactions of flexible polyelectrolytes in diluted solutions. [58] Conductometric measurements of Arabic gum [59] showed dependence with a minimum value of conductivity. Nelson explained this behavior on the base of the increase of the ions mobility due to the intermacromolecular interactions and the coiled backbones at high concentrations leading to the decrease of the number of the condensed conterions.

Electrolytic conductivity behavior of the systems of AgA/PNIPAM, AgA/PEG, AgA/ PAM in twice-distilled water is presented in figure 11. A curve with a minimum value of conductivity at a mixture composition of 36 % AgA / 64 %PNIPAM, 18 %AgA/ 82 % PEG and 18 %AgA / 82 %PAM was found that means at these compositions the H-bonding associations are formed. Conductometric results are in accordance with the viscometric and potentiometric results and there are comparable with results obtained by Betktutov [9] at titration of poly (acrylic acid) (PAA) with poly (vinyl pyrolidone) (PVP) in DMSO or DMF or by Ghimici [57] in the study of the conductivity dependence on polyelectrolyte concentration, charge density, substituent at the ionic group and solvent polarity.

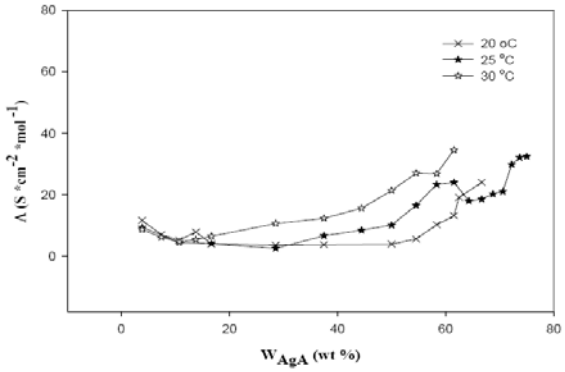

a

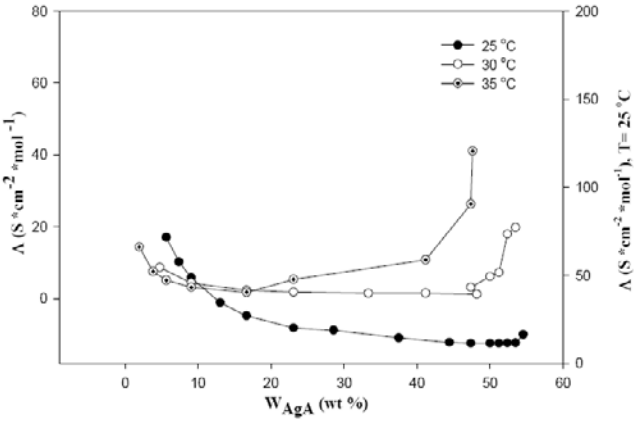

b

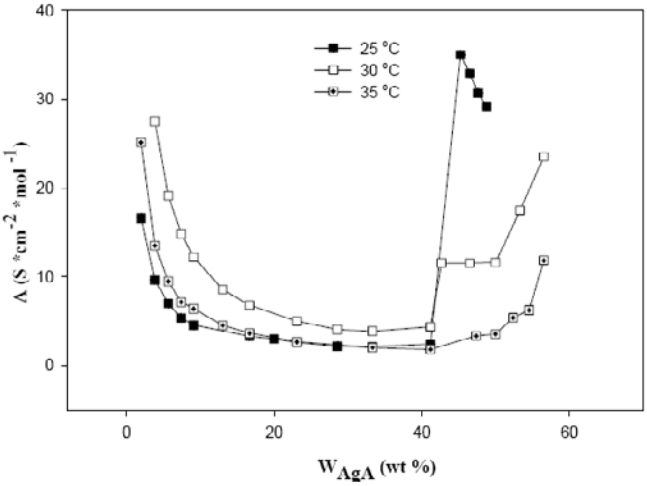

c

Figure 11. Molar conductivities of the systems AgA/PNIPAM (a) AgA/ PEG (b) in twice - distilled water, at different temperatures in function of composition.

CONCLUSIONS

It was established via viscometric measurements, pH determinations, and conductometry experiments that between alginic acid (AgA) and PNIPAM, PEG and PAM, interpolymeric associations with different conformations and different stabilities were formed.

It was studied the influence of temperature on the formation and stability of these associations and their thermodynamic characteristics like association degree, association (stability) constant, thermodynamic parameters have been evaluated.

pH studies had been performed at pH=4 which means the solubility limit of alginic acid (AgA). Therefore it can be appreciated that this limit is also available for the formation of the interpolymeric associations via hydrogen bonds however there are not excluded the presence of some ionic bonds. The most probable composition ranges found for the existence of these weak intermacromolecular associations is as follows:

System	Viscometry	Potentiometry	Conductometry
AgA/ PNIPAM	15- 70 % AgA/ 85-30% PNIPAM	16-70% AgA/ 84-30% PNIPAM	36 % AgA/ 64 %PNIPAM
AgA/ PEG	2-38 % AgA/ 98-62% PEG	15-45% AgA/ 90-55% PEG	18% AgA/ 82% PEG
AgA/ PAM	18-52 % AgA/ 82-48% PAM	15-45% AgA/ 90-55% PAM	18 %AgA/ 82% PAM

A good accordance between the results of the three used methods can be remarked.

REFERENCES

[1] G. Staikos, G.Bokias, G. G. Bumbu, Water soluble polymer systems- phase behaviour and complex formation, chapter 5 in *Handbook of Polymer Blends and Composites*, Vol 3A, C. Vasile, A. K. Kulshreshtha (Eds) , Rapra Technology Limited, Shawbury, 2003, 135-178.

[2] M. Jiang, M. Li, M. Xiang, H. Zhou, Interpolymer Complexation and Miscibility Enhancement by Hydrogen Bonding, *Adv. in Polym. Sci.*, 1999, 146: 121-196

[3] V. V. Khutoryanskiy, G. A Mun, Z. S Nurkeeva, A. V Dubolazov, pH and salt effects on interpolymer complexation via hydrogen bonding in aqueous solutions, *Polym. Int*., 2004, 53:1382–1387.

[4] Z. S. Nurkeeva, G. A. Mun, V. V. Khutoryanskiy, Interpolymer Complexes of Water-Soluble Nonionic Polysaccharides with Polycarboxylic Acids and Their Applications, *Macromol. Biosci*. 2003, 3: 283-295

[5] T. Ozeki, H. Yuasa, Y. Kanaya, Controlled release from solid dispersion composed of poly(ethylene oxide)–Carbopol interpolymer complex with various cross-linking degrees of Carbopol, *J. Controlled Release.* 2000, 63: 287-295.

[6] M. K. Chun, C. S. Cho , H. K. Choi, Mucoadhesive drug carrier based on interpolymer complex of poly(vinyl pyrrolidone) and poly(acrylic acid) prepared by template polymerization. *J. Controlled Release*, 2002, 81: 327-334.

[7] B. S. Lele, A. S. Hoffman, Mucoadhesive drug carriers based on complexes of poly (acrylic acid) and PEG-ylated drugs having hydrolysable PEG–anhydride–drug linkages. *J. Controlled Release*, 2000, 69:237-248.

[8] G. Colo, S. Falchi, Y. Zambito, In vitro evaluation of a system for pH-controlled peroral delivery of metformin, *J. Controlled Release*, 2002, 80:119-128.

[9] E. A. Betktutov, L.A. Bimmendina, Interpolymer Complexes, *Adv. Polym Sci*., 1981, 41:99-145.

[10] V. A. Prevysh, B. C. Wang, R. J. Spontak, Effect of added salt on the stability of hydrogen- bonded interpolymer complexes, *Colloid Polym. Sci*., 1996, 274:532-538.

[11] G. Staikos, K. Tsitsilianis, Viscometric investigation of the poly (acrylic acid)-polyacrylamide interpolymer association, *J. Appl. Polym. Sci*., 1991, 42:867- 872.

[12] G. Staikos, G. Bokias , C. Tsitsilianis, The viscometric methods in the investigation of the polyacid-polybase interpolymer complexes, *J. Appl. Polym. Sci.*, 1993, 48:215 – 217.

[13] E. Tsuchida, Y. Osada, H. Ohno, Formation of Interpolymer Complexes, *J. Macromol. Sci.- Phys., B*. 1980, 17:683-714.

[14] C. Vasile, G. G. Bumbu, Y. Mylonas, I. Cojocaru, G. Staikos, Hydrogen - Bonding interaction of an alternating maleic acid- vinyl acetate copolymer with poly (ethylene glycol), polyacrylamide and poly (N-isopropylacrylamide): a comparative study, *Polym. Int*, 2003, 52:1887-1891.

[15] G. G. Bumbu, J. Eckelt, C. Vasile, Interpolymeric Complexes Containing Copolymers in Hydrogen Bonded Interpolymer Complexes: Formation, Structure and Applications.V. V. Khutoryanskiy and G. Staikos Eds. *Elsevier* in press

[16] G. G. Bumbu, C. Vasile, Stimuli responsive copolymers of poly (maleic acid-alt-vinyl acetate) grafted with poly(N-isopropyl acrylamide). Influence of copolymer composition and of pH, *Memoriile Stiintifice ale Academiei Romane***:**In press.

[17] O. Nikolaeva, T. Budtova, V. Alexeev, S. Frenkel, Interpolymer association between polyacrylic acid and cellulose ethers: formation and properties, *J. Polym. Sci: Part B: Polym. Phys*., 2000, 38:1323-1330.

[18] C. Vasile, G. G. Bumbu, R. Dumitriu, G. Staikos, Comparative study of the behavior of carboxymethyl cellulose-g- poly (N-isopropylacrylamide) copolymers and their equivalent physical blends, *Eur. Polym. J*., 2004, 40:1209- 1215.

[19] C. Vasile, G. G. Bumbu, G. Staikos Carboxymethyl cellulose grafted poly (N-isopropylacrylamide) II) Influence of temperature and pH on the solution behaviour. *Cell. Chem. Technol*. In press.

[20] G. G. Bumbu J. Eckelt , C. Vasile, Interpolymer Complexes containing maleic copolymers. rheological behaviour, *European Polymer Congress, Portoroz, Slovenia, July* 2-6, 2007, P7.4.28.

[21] G. G. Bumbu, C. Vasile, G.C. Chitanu, G. Staikos, Interpolymer complexes between hydroxypropylcellulose and copolymers of maleic acid: A comparative study, *Macromol. Chem. Phys*., 2004, 206:540-546.

[22] G. Staikos, K. Karayanni, Y. Mylonas, Complexation of polyacrylamide and poly(N-isopropylacrylamide) with poly(acrylic acid). The temperature effect, *Macromol. Chem. Phys*. 1997, 198:2905

[23] C. Tapia, E. Costa, M. Moris, J. Sapag-Hagar, F. Valenzuela, C. Basualto , Study of the Influence of the pH Media Dissolution, Degree of Polymerization, and Degree of Swelling of the Polymers on the Mechanism of Release of Diltiazem from Matrices Based on Mixtures of Chitosan/Alginate, *Drug Development and Industrial Pharmacy*, 2002, 28:217-224.

[24] K. Y. Lee, W. H. Park, W. S. Ha, Polyelectrolyte complexes of sodium alginate with chitosan or its derivatives for microcapsules, *J. of Appl. Polym. Sci*, 1998, 63:425 – 432.

[25] A. Iruín, M. Fernández-Arévalo, J. Álvarez-Fuéntes, A. Fini, M. A. Holgado, Elaboration and “In Vitro” Characterization of 5-ASA Beads, *J. Drug Development and Industrial Pharmacy*, 2005, 31:231-239.

[26] J. I. Kadokawaa, S. Saitoub, S. I. Shodab, *Carbohydrate Polymers*, 2005, 60:253–258.

[27] Kenneth Clare, Algin, chapter 6 in *Industrial Gums*, Third edition,. R. L. Whistler, J.N. BeMiller (Ed), Academic Press, San Diego, 1993, 105

[28] http://www.arpc-ir.net/ PDF/ catalogue/ ChemicalSpec/Ethoxylates/PEG-Chemical %20Grade.pdf

[29] http://www.arpc-ir.net/PDF/catalogue/ChemicalSpec/Ethoxylates/PEG-Chemical%20Grade.pdf

[30] R. D. Lentz, I. Shainberg, R. E. Sojka , D. L. Carter, Preventing irrigation furrow erosion with small applications of polymers, *Soil Sci. Soc. Am. J*., 1992, 56:1926-1932.

[31] C. C. Shock, B. M. Shock, Comparative effectiveness of polyacrylamide and straw mulch to control erosion and enhance water infiltration in A. Wallace (Ed), *Handbook of Soil Conditioners*, M. Dekker Inc. New York, 1997, 429 – 444.

[32] C.C. Shock, E. B. G. Feibert, L. D. Saunders, S. Wimpy, H. Cox Treatment of soil with Bright Sun Soil Booster and polyacrylamide as soil conditioners for improved seedling emergence, *Malheur Experiment Station Special Report*, 1993, 924:199-200.

[33] W. M. Kulicke , J. Klein, *Angew Makromol. Chem*. 1987, 69: 169.

[34] H. Feil, Y. H. Bae, J. Feijen, S. W. Kim Effect of co-monomer hydrophilicity and ionization on the lower critical solution temperature of N-isopropylacrylamide copolymers, *Macromolecules*, 1993, 26: 496-250.

[35] X. Ma, J. Xi, X. Zhao, X. Tang, Deswelling comparison of temperature-sensitive poly (N-isopropylacrylamide) microgels containing functional OH groups with different hydrophilic long side chains, *J. Polym. Sci. Part B*: *Polym. Phys*, 2005, 43: 3575 – 3583.

[36] M. Heskins, J. E. Guillet, Solution properties of poly (N-isopropylacrylamide), *J. Macromol Sci A*, 1968, 2: 1441-1445.

[37] H. Ohno, K. Abe, E. Tsuchida, Solvent effect on the formation of poly(methacrylic acid)-poly(N-vinyl-2-pyrrolidone) complex through hydrogen bonding, *Makromol. Chem.*, 1978, 179: 755–763.

[38] G. R. Williams, B. Wright, Interactions in binary polymer systems, *J. Polym. Sci., Part A*, 1965, 3: 3885-3891.

[39] D. Staszewska, M. Bohdanecky, A viscometric study of dilute aqueous solutions of poly(vinylalcohol)-polyacrylamide mixtures, *Eur. Polym. J*., 1981, 17: 245-248.

[40] N. G. Belnikevich, T. V. Budtova, N. S. Nesterova, Y. N. Panov, S. Y. Frenkel, Applying the Viscosimetric Method of Determination of Intermolecular Interaction Constant for Probing Complex Formation, *Polym. Sci.*, 1992, 34: 3.

[41] G. Bokias, G. Staikos, I. Iliopoulos, R. Audebert, Interpolymer association between acrylic acid copolymers and poly(ethylene glycol) : effects of the copolymer nature, *Macromolecules*, 1994, 27: 427-431.

[42] G. G. Bumbu, C. Vasile, J. Eckelt, B. Wolf, Investigation of the Interpolymer Complex between Hydroxypropyl Cellulose and Maleic Acid-Styrene Copolymer, Dilute solutions studies, *Macromol, Chem. and Phys*, 2004, 205: 1869-1876.

[43] W. Kern, *Z. Phys. Chem*., A 1938, 181: 268.

[44] H. C. Trivedi, C. K. Patel, R. D. Patel, Studies on carboxymethylated cellulose: Potentiometric Titrations, *Makromol. Chem*., 1980, 182: 3561 – 3567.

[45] M. Nagasawa, S.A. Rice, A Chain Model for Polyelectrolytes. V. A Study of the effects of local charge density, *J. Amer.Chem. Soc*. 1960, 82: 5070.

[46] M. Koussathana, P. Lianos, G. Staikos, Investigation of Hydrophobic Interactions of Hydrogen- Bonding Interpolymer Complexes, *Macromol.*, 1997, 30: 7798-7802.

[47] E. Tsuchida, K. Abe Interactions between Macromolecules in Solution and Intermacromolecular Complexes, *Adv. Polym. Sci*., 1982, 45: 1–119.

[48] A. Marc, G. T. Van den Hoop, J. C. Benegas, Improvement in Conductometric Analysis of Metal/ Polyelectrolyte Systems, *Macromol.*, 1997, 30: 3930-3932.

[49] H. P. V. Leeuwen, R. F. M. J. Cleven, P. Valenta, Conductometric analysis of polyelectrolytes in solution, *Pure Appl. Chem*., 1991, 63: 1251-1268.

[50] H. E. Ricos, R.G. Barraza, I. C. Gamboa, Polyelectrolyte solutions. Electrical conductivity and counterion condensation, *Polym. Int*., 1993, 31: 213-216.

[51] H. L. Cheng, K.F. Lin, Molecular Weight Dependence of Chain Conformation and Counterion Dissociation of Poly(xylylene tetrahydrothiophenium chloride) in the Salt-Free Semidilute Aqueous Solutions, *Laugm.*, 2002, 18: 7287- 7290.

[52] H. Vink, Conductivity of polyelectrolytes in very dilute solutions, *J. Chem. Soc. Trans*., 1981, 77:2439.

[53] Z. Hu, S. Zhang, J. Yang, Y.Chen, Some properties of aqueous-solutions of poly(vinylamine chloride), J. *Appl. Polym. Sci.*, 2003, 89: 3889.

[54] H. Vink, Electrolytic conductivity of polyelectrolyte solutions, *Macromol. Chem.*, 1982, 183:2272-2283.

[55] L. Ghimici, S. Dragan, F. Popescu, Interaction of the low-molecular weight salts with cationic polyelectrolytes, *J. Polym. Sci. B*, 1997, 35: 2571- 2581.

[56] L. Ghimici, S. Dragan, Behaviour of cationic polyelectrolytes upon binding of electrolytes: effects of polycation structure, counterions and nature of the solvent, *Colloid Polym. Sci*., 2002, 280: 130-134.

[57] L. Ghimici, M. Nichifor, Electrical conductivity of some cationic polysaccharides. Effects of polyelectrolyte concentration, charge density, substituent at the ionic group and solvent polarity, *J.Polym. Sci., B*, 2005, 43: 3584-3590.

[58] C. Wandrey, D. Hunkeler, Study of Polyion Counterion Interaction. by Electrochemical Methods, chapter 5 in S. K. Tripathy, J. Kumar, H. S. Nalwa (Eds), *Handbook of Polyelectrolyte and Their Applications*, ACS Publisher, USA, 2002, 2: 147-172.

[59] R. Nelson, P. Ander, Electrical Conductivities of Salts of Gum Arabic and Carrageenan in Aqueous Solutions, *J. Phys. Chem*., 1971, 75: 1691-1697.